The Planetary Nebula System of M33

Robin Ciardullo[1], Patrick R. Durrell, Mary Beth Laychak[1], Kimberly A. Herrmann, Kenneth Moody

Department of Astronomy & Astrophysics, The Pennsylvania State University
525 Davey Lab, University Park, PA 16802

rbc@astro.psu.edu, pdurrell@astro.psu.edu, mary@cfht.hawaii.edu, herrmann@astro.psu.edu,
moody@astro.psu.edu

George H. Jacoby

WIYN Observatory, P.O. Box 26732, Tucson, AZ 85726

jacoby@wiyn.org

and

John J. Feldmeier[2]

Department of Astronomy, Case Western Reserve University
10900 Euclid Ave., Cleveland, OH 44106-1712

johnf@bottom.astr.cwru.edu

ABSTRACT

We report the results of a photometric and spectroscopic survey for planetary nebulae (PNe) over the entire body of the Local Group spiral galaxy M33. We use our sample of 152 PNe to show that the bright end of the galaxy's [O III] $\lambda5007$ planetary nebula luminosity function (PNLF) has the same sharp cutoff seen in other galaxies. The apparent magnitude of this cutoff, along with the DIRBE/IRAS foreground extinction estimate of $E(B-V) = 0.041$, implies a distance modulus for the galaxy of $(m-M)_0 = 24.86^{+0.07}_{-0.11}$ ($0.94^{+0.03}_{-0.05}$ Mpc). Although this value is $\sim 15\%$ larger than the galaxy's Cepheid distance, the discrepancy likely arises from differing assumptions about the system's internal extinction. Our photometry, which extends more than 3 mag down the PNLF, also reveals that the faint-end of M33's PN luminosity function is non-monotonic, with an inflection point ~ 2 mag below the PNLF's bright limit. We argue that this feature is due to the galaxy's large population of high core-mass planetaries, and that its amplitude may eventually be a useful diagnostic for studies of stellar populations.

Fiber-coupled spectroscopy of 140 of the PN candidates confirms that M33's PN population rotates along with the old disk, with a small asymmetric drift of ~ 10 km s^{-1}. Remarkably, the population's line-of-sight velocity dispersion varies little over ~ 4 optical disk scale lengths, with $\sigma_{\rm rad} \sim 20$ km s^{-1}. We show that this is due to a combination of factors, including a decline in the radial component of the velocity ellipsoid at small galactocentric radii, and a gradient in the

---

ratio of the vertical to radial velocity dispersion. We use our data to derive the dynamical scale length of M33's disk, and the disk's mass-to-light ratio. Our most likely solution suggests that the surface mass density of M33's disk decreases exponentially, but with a scale length that is ~ 2.3 times larger than that of the system's IR luminosity. The large scale length also implies that the disk's V-band mass-to-light ratio changes from $M/L_V \sim 0.3$ in the galaxy's inner regions to $M/L_V \sim 2.0$ at ~ 9 kpc. Models in which the dark matter is distributed in the plane of the galaxy are excluded by our data.

Subject headings: dark matter — distance scale — galaxies: distances and redshifts — galaxies: individual (M33) — galaxies: kinematics and dynamics — planetary nebulae: general

1. Introduction

For many years, H I and optical rotation curves have been used to establish the presence of dark matter halos around spiral galaxies (e.g., Faber & Gallagher 1979; Ashman 1992; Combes 2002). However, the mass profiles of these halos are still in doubt: from the rotation curves alone, it is impossible to decouple the gravitational contribution of the galaxy's visible disk mass from that of its dark halo (e.g., see Rubin 1997, and references therein). Most investigations begin with the assumption that a disk's mass-to-light ratio is constant with radius (e.g., Kent 1986; Palunas & Williams 2000; Sofue et al. 2003), but evidence in support of this hypothesis is limited. In fact, independent estimates of disk mass exist for only a handful of spirals (e.g., Bottema 1993; Bottema, van der Kruit, & Freeman 1987; van der Kruit et al. 2001; Gerssen, Kuijken, & Merrifield 1997, 2000), and in these systems, the data are restricted to the galaxies' inner ~ 2 scale lengths. Thus, while the information to date is consistent with the constant mass-to-light ratio hypothesis, the applicability of these studies to the dark-matter-dominated outer regions of spirals is limited.

The best way to independently determine the mass within a spiral's disk is through the motions of its old disk stars. However, the traditional approach to doing this via absorption-line spectroscopy is extremely challenging. Because the surface brightness of spiral galaxies declines exponentially with radius, observations at large radii are quite demanding and require intricate procedures for data reduction. This limits the effectiveness of the technique to the inner one or two disk scale lengths. Fortunately, there is an alternative. Instead of measuring the Doppler widths of integrated starlight, one can derive velocity dispersions directly from the motions of individual stars. Planetary nebulae (PNe) are the ideal targets for this purpose. PNe are excellent tracers of the galactic light (Ciardullo et al. 1989), easily identifiable via their strong [O III] $\lambda 5007$ emission and distinctive $I(5007)/I(H\alpha)$ ratio (Ciardullo et al. 2002), and measurable to a precision of a few km s^{-1} via medium dispersion spectrographs. Moreover, because the progenitors of PNe are intermediate and low mass stars, their velocity dispersion is representative of the old components of a galactic disk.

Here we describe a photometric and spectroscopic survey of the planetary nebula system of the Local Group spiral galaxy M33 (NGC 598). M33 is an excellent target for such an investigation. First, the galaxy is nearby, making large numbers of planetaries available for study. Second, since M33's photometric structure is well known at both optical (de Vaucouleurs 1959; Guidoni, Messi, & Natali 1981; Kent 1987) and infrared (Regan & Vogel 1994; Hippelein et al. 2003) wavelengths, information is available on the distribution of both the young and old stars of the system. Finally, M33's H I rotation curve is well-measured out to ~ 20 kpc (i.e., $\gtrsim 10$ disk scale lengths). Consequently, detailed models exist for the orientation of the galactic disk and the system's total potential (Rogstad, Wright, & Lockhart 1976; Corbelli & Schneider 1997; Corbelli & Salucci 2000).

We begin our study by describing our photometric survey of the galaxy, and comparing our [O III] $\lambda 5007$ and Hα PN measurements to those of Magrini et al. (2000, 2001). We demonstrate that there is generally good agreement between the samples, although our [O III] $\lambda 5007$ magnitudes are systematically brighter than the Magrini et al. (2000) values by ~ 0.12 mag. In Section 3, we present M33's [O III] $\lambda 5007$ planetary nebula luminosity function (PNLF) and show that at faint magnitudes, the function has the same non-monotonic behavior as the PNLF of the Small Magellanic Cloud. We interpret this turnover as a population effect and speculate on how the shape of the PNLF can be used to probe the mix of stellar populations within a galaxy. In Section 4, we use our data to derive a new PNLF-based distance to the galaxy, and discuss a possible reason for the $2\,\sigma$ difference between our measurement and that inferred from the galaxy's Cepheid variables.

After analyzing the photometric data, we describe our spectroscopic survey of the galaxy's planetary nebula system. In Section 5, we detail our observing and reduction procedures, and quantify the errors in our velocity measurements. In Sections 6 and 7, we use these data to examine the stellar kinematics of the galaxy. We present the system's line-of-sight velocity dispersion, estimate the stellar asymmetric drift, and use the epicyclic approximation to model the galaxy's velocity ellipsoid. We show that the line-of-sight velocity dispersion of M33's planetaries varies very little with galactic radius, and that this is due to a combination of factors, including a decline in the system's radial velocity dispersion at small galactocentric distances and a gradient in the ratio of the system's vertical to radial velocity dispersion. We also show that M33's vertical velocity dispersion decreases with a scale length that is greater than that of the galaxy's infrared light. In Section 8, we discuss possible systematic errors which may effect our result, including the variation of the PN scale height with galactocentric distance. Finally, we use our results to estimate the surface mass density of M33's disk, and constrain the radial profile of the galaxy's dark halo.

2. Identification of Planetary Nebulae

M33's PN candidates were identified on Kitt Peak 4 m telescope MOSAIC CCD images taken as part of the NOAO Local Group Galaxies survey program (Massey et al. 2002). This dataset consists of deep broad- ($UBVRI$) and narrow- ([O III], [S II], and Hα + [N II]) band images of 10 star-forming galaxies of the Local Group. Our program made use of the survey's M33 frames in [O III] $\lambda 5007$, Hα, B, and V. These data cover a $72' \times 36'$ region of the galaxy in three overlapping $36' \times 36'$ fields, and extend out to a radius of ~ 10 kpc, or four times the galaxy's disk scale length in blue light (de Vaucouleurs 1959). Our survey region is shown in Figure 1; the properties of the survey frames are summarized in Table 1.

To place the Massey et al. (2002) survey frames on a standard system, additional exposures in [O III] $\lambda 5007$ (900 s) and Hα (600 s) were taken with the same telescope/instrument setup on the UT nights of 2001 Dec 22 and 24. The seeing during these observations was moderately poor, $1''\!\!.4$ in [O III] and $1''\!\!.2$ in Hα, but the sky was photometric, and images of the Stone (1977) spectrophotometric standards BD+28 4211 and Feige 110 were acquired immediately before and after the exposures. These supplemental images were bias-subtracted, flat-fielded, and remapped onto the tangent plane using the `mscred` routines within IRAF (Valdes 1998). The latter two steps were performed after the iterative subtraction of the telescope's ghost pupil from the nights' dome flats.

PN candidates were identified by blinking the on-band [O III] $\lambda 5007$ and Hα survey images against their V-band counterparts. All spatially unresolved emission-line objects with little or no continuum flux were classified as planetary nebula candidates. Because medium band-width continuum images were not part of

the Massey et al. (2002) survey, this condition effectively meant that all PN candidates had to be either invisible in V, or have an instrumental $V - \lambda5007$ color less than ~ 3 (the ratio of the filters' bandpasses, corrected for transmission differences and the inclusion of [O III] $\lambda4959$ in the V filter). Since the seeing on the survey frames was generally very good, $\lesssim 1\rlap{.}''0$ (~ 4 pc) in [O III] $\lambda5007$ and $0\rlap{.}''8$ (or ~ 3 pc) in Hα, this simple classification scheme was generally unambiguous. To confirm the nature of the few sources with instrumental colors uncomfortably close to the discrimination threshold, i.e., with $2 < V - \lambda5007 < 3$, we also examined their appearance on the survey's B frames. Those objects with B-band fluxes close to that expected from a B main sequence star were classified as H II regions and eliminated from the analysis. We note that under these criteria, the two objects closest to our B-magnitude threshold are ~ 1.5 mag brighter in B than any other PN in our sample.

Once found, the PN candidates on each [O III] frame were measured astrometrically using a grid of ~ 200 reference stars from the USNO-A2.0 catalog (Monet et al. 1998). The formal internal errors of our plate solutions were $\sim 0\rlap{.}''3$ in both right ascension and declination. However, since M33's nuclear field overlapped the survey's northern and southern fields by 50%, almost two-thirds of our PN candidates appeared in two (or three) frames, and thus could be measured multiple times. The standard astrometric error between these measurements, $\sim 0\rlap{.}''15$, is slightly better than the internal errors of the individual plate solutions. This suggests that part of $\sim 0\rlap{.}''3$ scatter in the solutions comes from the proper motions of the reference stars, and that our relative astrometry is probably good to better than $\sim 0\rlap{.}''2$.

Relative [O III] $\lambda5007$ and Hα photometry of the PN candidates and several bright field stars was accomplished using the `daophot` point-spread-function fitting (PSF) routines within IRAF (Stetson 1987; Stetson, Davis, & Crabtree 1990; Stetson 1992). Our photometry was then checked by using `daophot`'s `substar` option to subtract off a scaled-PSF representation of each PN from its position on the frame. An examination of the residuals revealed that, while the vast majority of the subtractions were excellent, a few objects in or near the galaxy's spiral arms were slightly under- or over-subtracted, typically by ~ 0.1 mag. The cause of this error was an incorrect estimate of the galactic background, which (particularly in Hα) often included irregular H II regions, supernova remnants, and diffuse knots of emission. When this occurred, the PN magnitudes were manually adjusted until the residuals of the subtractions appeared reasonable.

After determining the raw PN instrumental magnitudes on each frame, the data were merged onto a common system by solving the least-squares condition required to match the magnitudes of stars in the regions of field overlap (Ciardullo et al. 1987). The instrumental magnitudes were then placed on the standard AB system by using the Dec 2001 data to compare large aperture measurements of field stars to similar measurements made of the Stone (1977) spectrophotometric standards. We estimate the error associated with this step to be ~ 0.03 mag. Finally, to transform the measured AB magnitudes to monochromatic fluxes, we blue-shifted the transmission curves of the [O III] $\lambda5007$ and Hα filters to correct for their temperature at the telescope, and applied the photometric procedures for emission-line objects described in Jacoby, Quigley, & Africano (1987) and Jacoby et al. (1989). In doing so, we assumed that M33's PNe have a mean heliocentric radial velocity of -180 km s^{-1} and a dispersion of ~ 85 km s^{-1} about that mean. Of course, the latter value is not strictly applicable to a rotating disk galaxy, but the error introduced by the peculiar velocity of an individual PNe is never more than 0.01 mag.

Table 2 lists the positions and emission-line strengths of our 152 PN candidates. The [O III] $\lambda5007$ magnitudes in the table are related to monochromatic flux by

$$m_{5007} = -2.5 \log F_{5007} - 13.74 \tag{1}$$

where the flux is given in ergs cm^{-2} s^{-1} (Jacoby 1989). Our typical photometric errors, as derived internally

from `daophot` and externally from objects with multiple measurements, are given in Table 3.

We note that a catalog of M33 PNe has previously been published (Magrini et al. 2000, 2001). The two datasets agree reasonably well. Except for a few anomalous outliers, the positions of PNe common to the two surveys are virtually identical: in right ascension and declination, our values are systematically larger than the Magrini et al. (2001) measurements by $0\overset{''}{.}07 \pm 0\overset{''}{.}06$ and $0\overset{''}{.}04 \pm 0\overset{''}{.}04$, respectively, and the overall dispersion between individual coordinates is $0\overset{''}{.}7$. Similarly, in Hα, there is little systematic difference between the photometry of the two surveys. On average, our Hα+[N II] log fluxes are 0.06 ± 0.05 mag fainter than those of Magrini et al. (2001), and, while the dispersion between the measurements is rather large (~ 0.25 mag for objects with log fluxes greater than -15), this may partly be due to the differing contributions of [N II] within the filters' bandpasses. In fact, the only significant difference between the two surveys is in the [O III] $\lambda 5007$ zero point. Although our [O III] $\lambda 5007$ magnitudes agree with those of Magrini et al. (2001) in the relative sense (the dispersion between the two measurements is ~ 0.1 mag for objects brighter than $m_{5007} \sim 23$), the zero point of our system is systematically brighter by 0.12 ± 0.05 mag. This offset and the dispersion between the measurements is shown in Figure 2.

Those Magrini et al. (2001) PN candidates that were not recovered in our survey are listed in Table 4, along with the probable reason for the discrepancy. The implied fraction of contaminants ($\sim 22\%$) is consistent with the 28% contamination rate estimated by Magrini et al. (2003) from follow-up spectrophotometry of the Hα, [N II], and [S II] lines of 36 PN candidates. However, we note that there are some discrepancies for individual objects. Specifically, Magrini et al. (2001) object #8, which is classified by Magrini et al. (2003) as a planetary nebula, is excluded from our sample on the basis of its detectable continuum emission and [O III] $\lambda 5007$ to Hα+[N II] line ratio (see below). Conversely, Magrini et al. (2001) objects #41 and 42 are included in our study, even though they are classified by Magrini et al. (2003) as probable supernova remnants.

Are all the PN candidates listed in Table 2 genuine? At M33's Cepheid distance of ~ 820 kpc (Freedman et al. 2001), our typical seeing of $1\overset{''}{.}0$ in [O III] $\lambda 5007$ and $0\overset{''}{.}8$ in Hα + [N II] implies that all H II regions or supernova remnants greater than ~ 3 pc in size are resolved. This is significantly better than the limit of ~ 7 pc associated with the poorer seeing exposures of the Magrini et al. (2000) survey, and as the catalog of Hodge et al. (1999) demonstrates, the density of H II regions in M33 decreases rapidly over this range. Moreover, since the Massey et al. (2002) survey frames reach a limiting magnitude of $V \sim 23.2$, all of M33's stars brighter than $M_V \sim -1.3$ are visible via their continuum. Consequently, unless an H II region is excited by a lone main sequence star with spectral type B3 or later, it will not make it into our sample. Finally, at the bright end of the [O III] $\lambda 5007$ luminosity function, the excitation properties of our objects demonstrate that the fraction of contaminants is negligible. As pointed out by Ciardullo et al. (2002), planetary nebulae inhabit a distinctive cone in [O III] $\lambda 5007$-Hα+[N II] emission-line space. While faint PNe (those more than ~ 3 mag down the [O III] $\lambda 5007$ luminosity function) can have [O III] $\lambda 5007$ to Hα + [N II] line ratios anywhere between $0.3 < R < 3$, PNe in the top ~ 1 mag of the PNLF all have $R \gtrsim 2$. This contrasts with the great majority of compact H II regions and supernova remnants, which typically have $R < 1$ (Shaver et al. 1983). As Figure 3 illustrates, *all* of our [O III]-bright PN candidates are high-excitation objects. Late-type B-stars cannot create nebulae with such high [O III] to Hα ratios: the central stars of all our candidates must be extremely hot, and optically faint. Taken together, the above arguments strongly suggest that the contamination fraction in our sample is extremely low.

3. The Planetary Nebula Luminosity Function

The top panel of Figure 4 displays M33's [O III] λ5007 planetary nebula luminosity function. The sharp cutoff at the bright end of the distribution is obvious, as is the function's slow decline at fainter magnitudes. Remarkably, both features are consistent throughout the galaxy. M33 has a sizable metallicity gradient (-0.11 ± 0.02 dex kpc^{-1}; Garnett et al. 1997), and the mean oxygen abundance of PNe in the galaxy's inner disk ($R < 15'$) is likely to be ~ 0.5 dex larger than that of PNe outside this radius. Yet, as the middle and lower panels of Figure 4 show, the [O III] λ5007 luminosity functions of the two samples are statistically identical. This constancy supports the conclusion of Ciardullo et al. (2002) that the PNLF cutoff is independent of metallicity for all but the most metal poor systems.

A second interesting feature exhibited in Figure 4 is the decline in the PNLF at magnitudes fainter than $m_{5007} \sim 22.5$. This roll over is partially real, and partially due to photometric incompleteness. To determine the effect of incompleteness, we began by excluding PNe located within $210''$ of the galaxy's nucleus; object detections in this region are difficult due to the bright, irregular features of the galactic background. We then measured the local sky associated with each remaining object, identified the worst (most uncertain) background in the sample, and computed the signal-to-noise each PN would have if it were projected on that background. Artificial star experiments have shown that PN identifications become incomplete when the signal-to-noise of a detection drops below ~ 10 (Ciardullo et al. 1987; Hui et al. 1993). Our putative signal-to-noise measurements therefore translate directly into a completeness limit. Our completeness limit, $m_{5007} \sim 23.75$, is more than a magnitude fainter than the point where the observed PNLF begins to decline.

We can confirm the reality of the dip at $m_{5007} \sim 23$ by comparing the radial distribution of "bright" PNe ($m_{5007} \leq 22.5$) to a similar distribution for PNe with $23.0 \leq m_{5007} \leq 23.75$. If incompleteness were important, then we might expect the latter sample to be missing PNe at small radii, where detections are more difficult due to the brighter surface brightness of the underlying galaxy. As Figure 5 (and the Kolmogorov-Smirnov statistic) show, this is not the case: outside of the inner $\sim 210''$, the cumulative radial distributions for "bright" and "faint" PNe are identical. The agreement between the two distributions demonstrates that our estimate of the detection limit is reasonable and the decline in the luminosity function at $m_{5007} \sim 23$ is real.

The decrease in the luminosity function at fainter magnitudes, though unexpected, is not difficult to explain. In fact, there are at least two possible mechanisms which, in theory, can produce a non-monotonic PNLF. The first is internal extinction in the host galaxy. The central extinction in M33 is $A_V \sim 0.9$ mag and there is a significant amount of dust distributed throughout the galaxy's disk (Regan & Vogel 1994; Hippelein et al. 2003). Because the scale height of PNe should be larger than that of the interstellar medium (Mihalas & Binney 1981), one would expect the bright end of the PNLF to be dominated by objects foreground to the dust layer. The observation of bright PNe above the dust lanes of the edge-on spirals NGC 891 (Ciardullo, Jacoby, & Harris 1991) and NGC 4565 (Jacoby, Ciardullo, & Harris 1996) support this idea. However, at fainter magnitudes, the contribution of extincted PNe may conceivably be enough to distort the shape of the PNLF and cause the observed luminosity function to turn over.

To investigate this possibility, we modeled the disk of M33 as an isothermal sheet of stars (scale height z_s) containing an embedded layer of dust (scale height z_d). We then adopted the analytic form of the PNLF proposed by Ciardullo et al. (1989)

$$N(M) \propto e^{0.307M}\{1 - e^{3(M^* - M)}\} \tag{2}$$

and performed a series of Monte Carlo experiments, in which the ratio of the two scale heights was allowed

to vary between $0.1 < z_d/z_s < 0.5$, and the total extinction ranged between $0.3 < A_V < 1.5$. In no case did the mixture of dust and stars produce a non-monotonic PNLF. If the layer of dust is thick enough and if the total amount of extinction is large, then both the number of PNe and the apparent magnitude of the PNLF cutoff may be affected by extinction. However, our analysis suggests that internal extinction, by itself, cannot turn the exponentially increasing PNLF of equation (2) into the peaked luminosity function displayed in Figure 4.

An alternative explanation for M33's PNLF comes from stellar evolution. According to the initial-mass final-mass relation (Weidemann 2000), old stellar populations produce low-mass central stars with evolutionary timescales much longer than the timescale for nebular expansion (Vassiliadis & Wood 1994). To a first approximation, such objects can be modeled as non-evolving central stars surrounded by freely expanding gaseous envelopes. The [O III] $\lambda5007$ emission of these PNe will decrease with time, t, following the relation

$$F_{5007} \propto N_O \, N_e \, V \propto N_e \propto \frac{1}{R^3} \propto \frac{1}{t^3} \qquad (3)$$

where N_O is the number density of O^{++} ions, N_e is the electron density, V, the volume of the nebula, and R, the nebular radius. For an ensemble of objects, the number of PNe with [O III] $\lambda5007$ magnitudes between M and $M + dM$ will then be

$$N(M_{5007}) \propto \frac{dt}{dm} \propto e^{0.307M} \qquad (4)$$

This is the exponential law first proposed by Henize & Westerlund (1963) and used by Ciardullo et al. (1989) in their PNLF calculations. However, it may not be applicable for younger stellar populations. In these systems, the typical planetary nebula will have a higher mass core, and a much shorter timescale for stellar evolution. If this timescale is comparable to, or shorter than, the timescale for envelope expansion, then a PN's [O III] $\lambda5007$ evolution will be driven by the luminosity evolution of its central star, rather than the expansion of its nebula. Since post-AGB stars spend a relatively long time at high luminosity (as they cross they HR diagram at the end of shell burning), a short time at intermediate luminosity (when nuclear reactions stop), and a long time at low luminosity (as their cooling rate slows), the PNLF of high-mass objects will be double-peaked, and similar to that calculated for post-AGB stars by Vassiliadis & Wood (1994).

Of course, in order to model real systems, one must include central star evolution, nebular expansion, and gas dynamics in the analysis, as well as the mix of stellar populations within a galaxy (see Marigo et al. 2004). Nevertheless, these simple arguments do explain the different PNLFs found in Local Group galaxies. As Figure 6 demonstrates, the low-mass stars of M31's bulge have a PNLF that is well-represented at the faint end by an exponential (Ciardullo et al. 2002). Conversely, M33 and the SMC are actively forming stars and their PNLFs are consistent with the bimodal distribution of Vassiliadis & Wood (1994). Given the distinctive nature of the two limiting cases, it is possible that the strength of the "dip" in the luminosity function may someday be a useful probe of stellar populations which are otherwise difficult to observe.

4. The Distance to M33

Although the shape of the PNLF at fainter magnitudes may change with time, the absolute magnitude of the function's bright-end cutoff stays amazingly constant (Jacoby et al. 1992; Ciardullo 2003). Whether this is due to convergence in the initial mass-final mass relation (Jacoby 1997), a fortuitous correlation between central star UV flux and circumstellar extinction (Ciardullo & Jacoby 1999; Ciardullo 2003), or the contribution of some other PN-like object (Marigo et al. 2004) is unclear. Nevertheless, the insensitivity of

the PNLF cutoff to population age and metallicity makes the feature extremely useful as an extragalactic standard candle.

To derive M33's PNLF distance and its formal uncertainty, we followed the procedures of Ciardullo et al. (1989). We took the analytic form of the PNLF given in equation (2), convolved it with the photometric error vs. magnitude relation of Table 3, and fit the resultant curve to the data via the method of maximum likelihood. Since this empirical law assumes a monotonically increasing PNLF at faint magnitudes, we limited the range of the fit to $m_{5007} < 22.5$. In addition, in order to correct for foreground Galactic extinction, we adopted the DIRBE/IRAS-based reddening value of $E(B - V) = 0.041$ (Schlegel, Finkbeiner, & Davis 1998) and used the relation of Cardelli, Clayton, & Mathis (1989) with $R_V = 3.1$ to go from differential to total $\lambda 5007$ extinction. Assuming an absolute magnitude for the PNLF cutoff of $M^* = -4.47$ (Ciardullo et al. 2002), the most likely distance to M33 is $(m - M)_0 = 24.86$ (0.94 Mpc) with a formal fitting error of $+0.05/-0.10$ mag. When we include the systematic errors associated with the observation's photometric zero point (0.03 mag), the filter response curve (0.03 mag), and the Galactic foreground extinction ($0.16\, E(B-V)$; Schlegel, Finkbeiner, & Davis 1998), M33's most likely PNLF distance modulus becomes $(m - M)_0 = 24.86^{+0.07}_{-0.11}$, or $0.94^{+0.03}_{-0.05}$ Mpc.

Our PNLF distance modulus of $(m - M)_0 = 24.86^{+0.07}_{-0.11}$ is 0.30 mag larger than M33's Cepheid distance modulus of 24.56 ± 0.10. If these uncertainties are accurate, then a simple propagation of errors (i.e., Bevington 1969) implies that the two measurements are discrepant at the $\sim 2\,\sigma$ level. There are two possible explanations for this discrepancy.

The first involves a metallicity dependence in either (or both) of the distance indicators. Thirteen galaxies have both PNLF and Cepheid distance measurements, and a detailed analysis of these data has been performed by Ciardullo et al. (2002). Their results are striking: except for the most metal-poor systems, the distance residuals are perfectly consistent with the internal uncertainties of the methods. Moreover, although a systematic shift is seen in low-metallicity ($[O/H] \lesssim -0.5$) systems, the offset is exactly that predicted for the PNLF by Dopita, Jacoby, & Vassiliadis (1992). This agreement leaves little room for further metallicity corrections in either the PNLF or Cepheid methods.

Nevertheless, since our distance estimate to M33 assumes $M^* = -4.47$, it is possible that metallicity does play a role in the distance discrepancy. However, in order to do so, the mean oxygen abundance of the PNe in our sample must be ~ 0.2 dex below that of the Large Magellanic Cloud. The data of Garnett et al. (1997) show that this is unlikely: only in the outermost regions of the galaxy do the H II region abundances drop to this level. Moreover, if M^* were being affected by metallicity, the strong abundance gradient across the galaxy would cause our measurement of m^* in M33's outer disk to be fainter than that of the inner disk. As Figure 4 demonstrates, this is not observed. In fact, the PNLF cutoff for the sample of PNe with $R > 15'$ is marginally brighter than that for the PNe inside this radius (by 0.15 ± 0.17 mag). This constancy strongly suggests that the low metallicity of M33 is not causing us to overestimate M^* and the distance to the galaxy.

As pointed out by Ciardullo et al. (2002), a more likely explanation for M33's distance discrepancy involves divergent assumptions about the galaxy's internal reddening. M33's Cepheid distance uses an extinction estimate that is derived from multicolor photometry of the Cepheids themselves (Freedman, Wilson, & Madore 1991; Freedman et al. 2001), while the PNLF method assumes the DIRBE/IRAS Galactic value. The difference between these values, $E(B - V) = 0.17$, is one of the largest observed for any Cepheid galaxy. If we were simply to adopt the Cepheid reddening estimate of $E(B - V) = 0.21$ (as did Magrini et al. 2000), or if the internal reddening were reduced to one typical of other Cepheid galaxies, the PNLF

and Cepheid distance indicators would be in much better agreement. Additional support for this hypothesis comes from the galaxy's red giant stars. The distance moduli derived by Kim et al. (2002) using the tip of the red giant branch (24.81 ± 0.04 (random) ± 0.13 (systematic)) and the location of the red clump (24.80 ± 0.04 (random) ± 0.05 (systematic)) are both consistent with the PNLF value.

5. Planetary Nebula Spectroscopy

The radial velocities of M33's planetary nebulae were measured with the WIYN telescope, the HYDRA bench spectrograph, and a 600 lines mm^{-1} grating blazed at 10°1 in first order. Most of the PNe were observed on the photometric nights of 2002 Oct 3-5, with the 2″ red fiber cable and a telescope-instrument combination which produced spectra with 2.8 Å (168 km s^{-1}) resolution and 1.4 Å pixel^{-1} dispersion over the wavelength range between 4500 Å and 7000 Å. The data were taken using six fiber setups, each of which targeted ~ 50 PNe with ~ 5 fibers devoted to the sky. The total exposure time for each setup was ~ 3.5 hours, and, in order to allow for the removal of cosmic rays and other instrumental artifacts, the integrations were subdivided into a series of 30 min exposures. To provide a check on the repeatability of the measurements, $\sim 75\%$ of the PNe were observed multiple times, and 7 PNe, ranging in brightness between $21.0 < m_{5007} < 25.0$ were targeted in four or more setups.

To supplement these data, additional spectra for 24 PN candidates were obtained by R. Chandar and H. Ford on the nights of 2003 Jan 3-5 using HYDRA's 3″ blue fiber cable and a 400 lines mm^{-1} grating blazed in first order at 4°2. These data, which covered the wavelength range between 3660 Å and 6860 Å, had a slightly lower dispersion than the Oct 2002 data (~ 6 Å resolution at 1.56 Å pixel^{-1}), but longer (~ 5 hr) exposure times partially compensated for this drawback. These Jan 2003 observations yielded three additional PN velocities, and reduced the measurement errors of 21 other objects.

Data reduction was accomplished with the `dohydra` task within IRAF. Flat-fielding was performed using dome flat exposures obtained at the beginning of each night, and wavelength calibrations were found using a series of CuAr comparison arcs taken before, during, and after the science exposures of each setup. The solutions derived from these comparison arcs had a rms dispersion of ~ 0.03 Å (~ 2 km s^{-1}) and were stable throughout each setup. Next, the spectra were linearized to a common wavelength scale, and sky subtracted using an average sky spectrum determined from the setup's sky fibers. Because our observations focussed on regions of the spectrum well away from any airglow emission, and were performed during dark time at moderately high ($R \sim 2000$) dispersion, the details of this subtraction make very little difference to the final result. After sky subtraction, the individual exposures of each setup were co-added and shifted into the barycentric rest frame to produce a single summed spectrum for each object.

PN radial velocities were derived in a two step process. First we obtained an interim velocity for each PNe using the centroids of the bright emission lines of [O III] $\lambda\lambda 4959, 5007$, H$\alpha$, H$\beta$, and (when possible) [N II] $\lambda\lambda 6548, 6584$. We then used these velocities to create an ultra-high signal-to-noise PN template by shifting all of the spectra into the rest frame and co-adding the data. Using this template, we then determined our final PN velocities by cross-correlating the individual spectra against the template spectrum with the `xcsao` task of the `rvsao` package (Kurtz & Mink 1998) of IRAF. Generally speaking, for faint emission-line objects, velocities derived in this way are slightly more accurate than velocities found from the weighted average of individual emission-line measurements. In the case of our M33 survey, where most of the PNe are bright, the improvement to our measurements was marginal. The mean difference between velocities determined via cross-correlation and those found by the line-centroiding (`emsao`) task within `rvsao` was only

$+0.15 \pm 0.34$ km s^{-1}.

At this stage, we verified the internal consistency of our velocity measurements by cross-correlating the spectra of each individual setup against the template spectrum, and intercomparing the results for the 113 PNe with multiple measurements. Table 5 summarizes the results of this analysis by listing the mean velocity offset of each setup with respect to the others, and the number of velocity pairs used to derive these values. From the table, it is clear that systematic setup-to-setup velocity differences are minimal: the only setup whose offset is not consistent with zero is that of Setup 4, and its velocities are low by only ~ 2.9 km s^{-1}. Table 5 also lists the standard error between the individual pairs of PN measurements. This error provides an upper limit to the internal accuracy of our measurements.

Column 10 of Table 2 lists our velocity measurements for M33's PNe. Column 9 of the table gives the number of fiber setups employed for each object, excluding the observations of January 2003. Those PNe targeted in January are identified in Column 13, and their velocities are the weighted mean of the results from the two observing runs. In total, of the 152 PN candidates identified on our survey frames, 151 were targeted by WIYN, and 140 were detected via their emission lines. (Of the 11 objects that were not detected, 7 are extremely faint.) Note that the errors quoted in Column 8 are the internal uncertainties of the cross-correlation technique and do not include any setup-to-setup systematic uncertainty. As demonstrated in Table 5, such errors are small, $\lesssim 3$ km s^{-1}.

6.   The M33 Planetary Nebula Velocity Field

The large scale velocity distribution of M33's PNe is illustrated in Figure 1. The most obvious feature displayed in the figure is the galaxy's rotation. M33 is inclined $\sim 56°$ to the line-of-sight (see Zaritsky, Elston, & Hill 1989, and references therein), and this inclination is reflected in the radial velocities of the planetaries. In fact, since M33's spheroid-to-disk ratio is extremely small, $S/D \sim 0.02$ (Bothun 1992; Regan & Vogel 1994), all but ~ 2 PNe should be rotating along with the galactic disk.

To explore the dynamics of M33's PN population, we began by assuming that, in the mean, the system's PNe are confined to the disk and move in circular orbits about the galactic nucleus, which is at $\alpha(2000) = $ 1:33:50.915, $\delta(2000) = +30$:39:36.79 (Massey et al. 1996). We then defined the inclination and orientation of this disk. On average, M33 is inclined $i \sim 56°$ to the line-of-sight and has a major-axis position angle of $\theta = 23°$ (Kent 1987; Zaritsky, Elston, & Hill 1989); these values are consistent with the isophotal contours of the inner parts of the galaxy (Kent 1987), as well as the kinematics of the system's H II regions (Zaritsky, Elston, & Hill 1989). However, such a model is probably too simplistic. The kinematics of M33's H I gas demonstrates the presence of a significant warp in the galaxy's outer regions (Rogstad, Wright, & Lockhart 1976; Corbelli & Schneider 1997; Corbelli & Salucci 2000). This warping is also confirmed by the asymmetrical shape of the galaxy's spiral arms (Sandage & Humphreys 1980). To include this effect, we therefore adopted the model of Corbelli & Salucci (2000), in which the inclination and position angle of M33's disk varies with galactocentric distance. Fortunately, our analysis depends very little on the details of this assumption: over the inner $\sim 30'$ of the galaxy (i.e., over most of our survey region), the difference between the Corbelli & Salucci (2000) model and the simple $i = 56°$ $\theta = 23°$ geometry is slight (no more than $4°$ in inclination and $5°$ in position angle). Nevertheless, since M33's warp does become important outside this range, and since a few of our PNe do have large isophotal radii, we prefer this approach over the less sophisticated flat-disk assumption.

After defining M33's inclination and position angle, we deprojected the position of each PN to determine

its galactocentric radius (R) and position angle with respect to the galaxy's major axis (ϕ). The rotation speeds of the PNe, V_*, were then inferred from the line-of-sight radial velocities, $V_{\rm rad}$, via

$$V_* = \frac{(V_{\rm rad} - V_{\rm sys})}{\sin i \, \cos \phi} \qquad (5)$$

For the systematic velocity, we used $V_{\rm sys} = -180$ km s^{-1}; this value is based on both radio (de Vaucouleurs et al. 1991) and optical (Huchra, Vogeley, & Geller 1999) observations of the galaxy, and is comfortably close to the mean radial velocity of $\langle V_{\rm rad} \rangle = -176$ km s^{-1} found from the PNe of this study.

The top panel of Figure 7 compares our PN rotational velocities with the rotation curve of M33's atomic (H I) and molecular (CO) gas (Corbelli 2003). All objects except 14 PNe within $10°$ of the minor axis have been plotted. Overall, the agreement is quite good. The data display some amount of scatter, but this is due to the peculiar radial, tangential, and vertical velocities of the PNe. When these non-circular motions are amplified by the $\cos \phi$ division, the result is the dispersion seen in the figure. Also apparent is the small, but significant, offset between the mean circular velocity of the PNe and the rotation speed of the gas. The bottom panel of the figure shows this offset more clearly by binning the data by galactocentric radius with 18 objects per bin. The amplitude of the velocity lag, or asymmetric drift, is ~ 10 km s^{-1}, less than half the drift velocity observed for old-disk stars in the vicinity of the Sun (Ratnatunga & Upgren 1997; Dehnen & Binney 1998). However, since the ratio of M33's drift speed to rotation velocity is approximately the same as that for the solar neighborhood, our measurement suggests that the dynamical state of M33's disk is not too dissimilar to that of the Milky Way. We will return to the issue of asymmetric drift in Section 7, where we use it to help constrain the shape of the system's velocity ellipsoid.

Another way to examine the motion of M33's PNe is to plot their line-of-sight velocities after removing the contribution of the rotating stellar disk (defined as the H I + CO gas velocity minus the asymmetric drift). This is done in Figure 8; the top panel of the figure shows the individual PN velocities, while the lower panel bins the velocities to show the line-of-sight velocity dispersion. The figure again demonstrates that the non-circular motions of the PNe are significant, with $\sigma_{\rm rad} \sim 25$ km s^{-1}. This is more than twice the 9 ± 4 km s^{-1} dispersion found for the galaxy's H II regions (Brandt 1965; Zaritsky, Elston, & Hill 1989). In addition, our innermost measurement of $\sigma_{\rm rad} = 22^{+5}_{-3}$ km s^{-1} is very close to the galaxy's central value of 24.0 ± 1.2 km s^{-1} found from absorption line spectroscopy (Gebhardt et al. 2001). Since M33 shows no dynamical evidence for a central black hole or mass concentration, this agreement confirms that we are, indeed, measuring a velocity dispersion that is representative of old disk stars.

Figure 8 also supports our contention that there are very few non-disk PNe in our sample. Of the 140 PNe surveyed, only two objects, PN 67 and PN 24, have velocities that are more than $2.3\,\sigma$ from the galactic rotation. These planetaries, which deviate by 2.8 and $3.0\,\sigma$ respectively, may *possibly* belong to M33's spheroidal component. On the other hand, in a normally distributed population of 140 PNe, we should expect to find ~ 2 objects with velocities more than $\sim 2.5\,\sigma$ away from the mean. Thus, it is possible that *none* of our PNe belong to M33's halo, and all are rotating along with the disk. This confirms the photometric results of Bothun (1992), Regan & Vogel (1994), and Tiede, Sarajedini, & Barker (2004) that M33's spheroidal component is negligible compared to its disk.

The most surprising aspect of Figure 8 is how little the line-of-sight velocity dispersion depends on galactocentric distance. In the K-band, where internal extinction presumably is unimportant, M33's disk scale length is $\sim 5\rlap{.}'8$ (Regan & Vogel 1994). Our observations, which extend out to a distance of $34'$, therefore sample ~ 6 scale lengths of the galaxy. If M33's disk is isothermal, then the galaxy's vertical velocity dispersion should decline significantly over this range. Specifically, if z_0 is the scale height of the

planetaries and Σ the disk-mass surface density, then under the isothermal disk approximation

$$\sigma_z^2(R) = \pi G \, \Sigma(R) z_0 \tag{6}$$

Since M33's stellar and gas surface density both decline exponentially (Guidoni, Messi, & Natali 1981; Regan & Vogel 1994; Corbelli 2003), it is reasonable to expect Σ, and therefore σ_z^2, to do the same. Unless the shape of the galaxy's velocity ellipsoid changes dramatically, or M33's disk is significantly flared, σ_{rad} should decrease by more than a factor of 20 over our survey region. Figure 8 clearly demonstrates that it does not.

7. Modeling the Velocity Ellipsoid

Because the disk of M33 is inclined $\sim 56°$ to the line-of-sight, peculiar stellar motions in the radial (σ_R), tangential (σ_ϕ), and vertical (σ_z) directions all contribute to the scatter seen in Figure 8. Specifically, the line-of-sight velocity dispersion is related to the galaxy's velocity ellipsoid through

$$\sigma_{\mathrm{rad}}^2 = \sigma_R^2 \sin^2 \phi \, \sin^2 i + \sigma_\phi^2 \cos^2 \phi \, \sin^2 i + \sigma_z^2 \cos^2 i \tag{7}$$

Consequently, in order to interpret the figure, the shape of M33's velocity ellipsoid needs to be constrained.

To do this, we began by using the epicyclic approximation to write σ_ϕ in terms of σ_R

$$\sigma_\phi^2 = \sigma_R^2 \left(\frac{1}{2} + \frac{1}{2} \frac{\partial \ln V_c}{\partial \ln R} \right) \tag{8}$$

(Binney & Tremaine 1987), where the circular rotation velocity, V_c, is known from the motion of the system's H I gas. We then parameterized equation (7) in terms of the two remaining unknowns, σ_z and σ_R, and, for each radial bin, we computed the relative probability of observing the given set of PN velocities as a function of these two variables. Once these probabilities were established, we normalized their values to one to generate the likelihood of each solution.

Note that this type of calculation requires that limits be placed on the variables, so that outside the range of analysis, the probability of a solution is identically zero. For σ_z, our analysis included all values between $0 < \sigma_z < 100$ km s^{-1}; given the ~ 100 km s^{-1} rotation speed of the galaxy, the true value of σ_z certainly falls within this range. Our choice of limits for σ_R was more difficult. In the vicinity of the Sun, the ratio of the vertical to radial velocity dispersion for old disk stars is $\sigma_z/\sigma_R \sim 0.5$ (Bienaymé 1999), and surveys of other spirals consistently find ratios in the range $0.3 < \sigma_z/\sigma_R < 0.9$ (e.g., Gerssen, Kuijken, & Merrifield 1997, 2000; Bottema 1993; van der Kruit & de Grijs 1999). Unfortunately, almost all these data are for stars between ~ 1 and ~ 2 disk scale lengths from the galactic center: there are no measurements of σ_R or σ_z over the entire range of radii considered in this paper. Thus, our only guidance on the shape of M33's velocity ellipsoid comes from numerical simulations. According to the models of Villumsen (1985) and Jenkins & Binney (1990), disk heating by molecular clouds and spiral structure should drive an initially isotropic velocity dispersion towards values of σ_z/σ_R as low as ~ 0.4. For a lower limit on σ_R, we can therefore demand that $\sigma_R > \sigma_z$. For the upper limit on this quantity, we can use the requirement that M33's disk be stable against buckling instabilities, which occur when $\sigma_z/\sigma_R \lesssim 0.3$ (Toomre 1966; Araki 1985; Merritt & Sellwood 1994). To be slightly conservative, we therefore limited our analysis to $0.25 < \sigma_z/\sigma_R < 1.0$.

Figure 9 displays the likelihood contours produced by our data. As is obvious from the figure, σ_R is better constrained than σ_z. This is understandable: not only did our boundary conditions ensure that $\sigma_R > \sigma_z$, but the former variable also receives the contribution of σ_ϕ, via the epicyclic approximation. As a

result, the line-of-sight velocity dispersion largely reflects the behavior of σ_R; our limits on σ_z come primarily from the constraints placed on the shape of the velocity ellipsoid, and secondarily from the fits.

The more important property shown in Figure 9 is the absence of an obvious radial gradient. There is very little difference between the fits for PNe near the center of M33 and PNe at $\gtrsim 4$ disk scale lengths. If the shape of the galaxy's velocity ellipsoid is roughly constant with radius, then the data imply that σ_z must also be very nearly constant. On the other hand, if the vertical velocity dispersion truly declines with radius (as it must in a constant mass-to-light ratio disk), the dispersion ratio σ_z/σ_R must also decline.

To make further progress, we can apply two additional constraints to our data. The first is the requirement that M33's disk be stable. According to Toomre (1964), in order for a thin stellar disk to be stable against axisymmetric perturbations, its radial velocity dispersion must satisfy the condition

$$\sigma_R > \frac{3.36\,G\,\Sigma}{\kappa} \tag{9}$$

where the epicyclic frequency, κ, is obtainable from the rotation curve via

$$\kappa = \frac{V_c}{R}\left(2 + 2\,\frac{\partial \ln V_c}{\partial \ln R}\right)^{1/2} \tag{10}$$

(Binney & Tremaine 1987). In addition, for stability against non-axisymmetric perturbations (i.e., bar formation), the disk must also satisfy the (slightly more stringent) condition

$$\sigma_R > \frac{3.36\,G\,\Sigma}{\kappa} \cdot \frac{2V_c}{R\,\kappa} \tag{11}$$

(Morosov 1980, 1981a,b). If we combine this equation with the isothermal disk approximation given by equation (6), we obtain a constraining relationship between the vertical and radial velocity dispersions

$$\sigma_z < \kappa\left(\frac{\pi z_0 R\,\sigma_R}{6.72\,V_c}\right)^{1/2} \tag{12}$$

To use this relation, we need to know z_0, the scale height of PNe in M33's disk. Our probability contours of Figure 9, in combination with the buckling instability condition, allow us to exclude values of $z_0 \lesssim 90$ pc in M33's outer regions ($R > 6$ kpc). To improve upon this number, however, we must turn to other galaxies. In the Milky Way, measurements of z_0 are notoriously uncertain, with published values ranging all the way from 90 pc to 300 pc (e.g., Pottasch 1984; Maciel 1989; Zijlstra & Pottasch 1991; Corradi & Schwarz 1995; Phillips 2003). Unfortunately, in other galaxies the situation is worse: internal extinction in the planes of edge-on galaxies make reliable measurements of the PN distribution nearly impossible (see Ciardullo, Jacoby, & Harris 1991; Jacoby, Ciardullo, & Harris 1996). For lack of a better alternative, we were therefore forced to adopt an intermediate value of $z_0 \sim 175$ pc as the most-likely scale height of our test particles. This value has two justifications. First, a Milky Way scale height of $z_0 \sim 175$ pc implies a vertical PN distribution similar to that of Galactic main-sequence F-stars (Mihalas & Binney 1981) and a total PN population that is consistent with PN observations in other galaxies (Peimbert 1993). Second, Bizyaev & Mitronova (2002) have found a correlation between the infrared (K_s) central surface brightness of a galaxy and the ratio between the galaxy's vertical and radial scale lengths. If one applies this relation to M33 (Regan & Vogel 1994) and normalizes the result using the ratio of our Galaxy's PN scale height to the total "old thin disk" scale height (Chen et al. 2001), then z_0 again becomes ~ 175 pc. Obviously, this value carries a substantial uncertainty of at least $\sim 25\%$.

We note that, in theory, the scale height of a galactic disk may change with radius. If it does, then the effect of the stability criterion will also have a radial dependence. In practice, however, this is not of great concern. Numerous studies of late-type edge-on spirals in the optical and infrared (e.g., van der Kruit & Searle 1982; Shaw & Gilmore 1990; de Grijs & van der Kruit 1996; de Grijs & Peletier 1997; Fry et al. 1999; Bizyaev & Mitronova 2002) have found that radial variations in the vertical scale heights of stars are always small, $\lesssim 10\%$. This is true even when the galaxies are tidally interacting: a study by Schwarzkopf & Dettmar (2001) shows that the fractional variation of z_0 in disturbed edge-on systems is typically less than 14%. Thus, even if M33's disk is warped at large radii, our assumption of a constant value for the scale height should be acceptable.

The solid lines of Figure 9 show the effect the stability requirement has on our probability contours. In the inner regions of the galaxy, the requirement is satisfied almost everywhere: virtually all the solutions lie below the stability cutoff. However, at large radii, the criterion severely limits the allowable values for the vertical velocity dispersion. Such an effect is unavoidable: if M33's disk is stable and isothermal, then the vertical velocity dispersion at large distances from the nucleus must be small.

Figure 10 applies the stability criterion and marginalizes Figure 9's remaining probability contours over the parameters σ_R (the middle panel) and σ_z (the lower panel). The top panel of the figure shows the behavior of σ_z if one asserts that M33's stellar disk is at the limit of stability; this solution also represents the largest values of σ_z possible under the isothermal disk approximation. In the figure, we have illustrated the shapes of the non-Gaussian errors via the widths of the shaded areas. The figure contains several features of note.

First, as anticipated, the requirement of stability produces a radial gradient in the vertical velocity dispersion. Remarkably, this gradient is much shallower than that expected from a constant mass-to-light ratio disk. In the V-band, M33's disk scale length is $\sim 9\farcs1$ (Guidoni, Messi, & Natali 1981); in the infrared, where the effects of extinction gradients are less, the scale length shrinks to $\sim 5\farcs8$ (Regan & Vogel 1994). Our kinematic measurements imply a physical scale length for M33's disk that is $\sim 13'$ or ~ 3.5 kpc. This scale length does not change much, even if one requires that the disk be pressing the limits of stability.

The other notable feature of Figure 10 is the behavior of the radial component of M33's velocity ellipsoid. Outside of ~ 2.5 kpc, σ_R declines with a scale length that is more than 3 times greater than that of the galaxy's optical light; this is slightly larger than the scale length one would expect from the survey data of Bottema (1993), but not exceptionally so. However, inside of ~ 2.5 kpc, σ_R levels off, and may even decline at small galactocentric radii. Although such behavior is not common, neither is it unique: the line-of-sight velocity dispersions of NGC 3198 and NGC 6503 suggest that these galaxies also have low central values of σ_R (Bottema 1993).

The turnover of M33's radial velocity dispersion is most likely a manifestation of the requirement that σ_R be much less than the galaxy's rotation speed. M33's rotation velocity increases from zero near the galactic center to ~ 90 km s^{-1} at ~ 3 kpc. If σ_R did not turn over, it would dominate galactic rotation within ~ 1.5 kpc of the nucleus, and the result would be a "hot" stellar population in the galaxy's central regions. If such a population exists in M33, it is extremely weak (Bothun 1992; Regan & Vogel 1994).

The turnover of the radial velocity dispersion explains why the system's line-of-sight dispersion is so flat: the increase in σ_z near the center of the galaxy is offset by the decline in σ_R. This flattening, however, does not affect the large scale trend in the dispersion ratio. In the interior of the galaxy, $\sigma_z/\sigma_R \sim 0.6$; by ~ 9 kpc, the ratio has dropped to $\lesssim 0.4$. This range of values is consistent with the numerical models of disk heating computed by Villumsen (1985) and Jenkins & Binney (1990). More importantly, our inferred

σ_z/σ_R gradient agrees with the analytic results of Carlberg (1987), who showed that the velocity ellipsoid of a disk must become rounder as the stellar velocity dispersion increases. Our recovery of this result supports the validity of our σ_z-σ_R decomposition.

There is one more constraint that can be applied to M33's stellar kinematics. From the Jean's equation, the rotational velocity of stars in a stellar disk is related to the circular velocity of the system's gas by

$$V_c^2 - \langle V_* \rangle^2 = \sigma_R^2 \left(\frac{\sigma_\phi^2}{\sigma_R^2} - 2\frac{\partial \ln \sigma_R}{\partial \ln R} - \frac{\partial \ln \nu}{\partial \ln R} - 1 \right) - R\frac{\partial \sigma_{Rz}}{\partial z} - \frac{R}{\nu}\frac{\partial \nu}{\partial z} \tag{13}$$

where ν is the stellar density (Binney & Tremaine 1987). If we use the epicyclic approximation, and assume that M33's PNe are scattered throughout a constant scale height isothermal disk, then this equation for asymmetric drift simplifies to

$$V_c^2 - \langle V_* \rangle^2 \simeq \sigma_R^2 \left(\frac{1}{2}\frac{\partial \ln V_c}{\partial \ln R} - 2\frac{\partial \ln \sigma_R}{\partial \ln R} - 2\frac{\partial \ln \sigma_z}{\partial \ln R} - \frac{1}{2} \right) \tag{14}$$

This equation, when combined with a model for the radial dependence of σ_z and σ_R, places a further constraint on M33's galactic kinematics.

Based on the galaxy's luminosity profile and the data displayed in Figure 10, it is reasonable to parameterize the radial dependence of M33's vertical velocity dispersion with a simple exponential of scale length R_z. An exponential function with scale length R_R can also be used to fit the galaxy's radial velocity dispersion, as long as the measurements are restricted to galactocentric distances greater than ~ 2.5 kpc. Inside this radius, however, the exponential law breaks down, and the form of the σ_R vs. R relation is unknown.

Rather than guess the radial dependence of σ_R in M33's inner regions, we elected instead to exclude from the analysis all measurements of σ_R and asymmetric drift within 2.5 kpc of the nucleus. This allowed us to parameterize the radial dependence of both σ_z and σ_R with exponentials and re-write (14) as

$$V_c^2 - \langle V_* \rangle^2 \simeq \sigma_R^2 \left(\frac{2R}{R_z} + \frac{2R}{R_R} - \frac{1}{2} + \frac{1}{2}\frac{\partial \ln V_c}{\partial \ln R} \right) \tag{15}$$

Using this equation, we simultaneously solved for the values of R_z, R_R, $\sigma_R(R=0)$, and $\sigma_z(R=0)$ which best fit both the velocity dispersions of Figure 10 and the asymmetric drift data of Figure 7. To perform this fit, we minimized the χ^2-like statistic

$$\chi^2 = -2 \sum_i \ln \left\{ \frac{P(y_i)}{P(y_m)} \right\} \tag{16}$$

where $P(y_i)$ is the probability of observing value y_i from a probability distribution P, and $P(y_m)$ is the probability of observing the most-likely value. This statistic, which reduces to the standard χ^2 value for normally distributed errors, enabled us to consider the non-Gaussian uncertainties associated with σ_R and σ_z, and the asymmetric drift errors in a consistent manner. It also permitted us to estimate the uncertainties in our scale lengths via a modified jackknife analysis. In this procedure, we repeatedly removed one planetary nebula at random from each of the bins, and re-fit the data. When analyzed in this way, the best fit scale length for σ_z^2 became $13.'5$ (with 90% of the simulations lying between $12.'2$ and $14.'9$), and the most likely value for the scale length of σ_R was $33.'5$ (with 90% of the simulations between $30.'5$ and $38.'6$). The results do not change much if one forces the disk to marginal stability: under this condition, the derived scale length of σ_z^2 declines by less than $\sim 5\%$. Once again, these scale lengths are significantly larger than the $5.'8$ value found from K-band photometry. In fact, our 3σ limits on M33's dynamical scale length lie between $10.'8$

and $16\!'\!0$, and none of our 20,000 simulations produced a scale length as low as the galaxy's optical scale length of $9\!'\!1$. Our best fit solution is illustrated in Figures 7b and 10 by dotted lines.

If the disk of M33 is indeed isothermal, then we can substitute the vertical velocity dispersions of Figure 10 into equation (6) to produce estimates for the galaxy's disk mass surface density. These densities can then be combined with optical (Guidoni, Messi, & Natali 1981) and infrared (Regan & Vogel 1994) surface photometry to generate values for the total disk mass-to-light ratio. Finally, we can remove the contribution of M33's interstellar medium from the mass-to-light values by subtracting the surface mass density of galactic H I and H_2 gas (Heyer et al. 2004) from the total mass density, and applying a first-order correction for internal extinction, using the central extinction value ($A_V = 0.9$ mag) and extinction scale length ($\sim 10\!'\!2$) derived by Regan & Vogel (1994). These mass estimates and mass-to-light ratios are presented in Table 6.

The errors quoted in Table 6 reflect only the formal uncertainties associated with our measurement of σ_z; not included are the systematic errors associated with our adopted value of z_0 and the use of the isothermal disk approximation. The former uncertainty is small: a 25% increase in the PN scale height (from 175 pc to 220 pc) results in only a $\sim 5\%$ decrease in the derived values for M33's disk mass surface density and scale length.

The error associated with the isothermal disk approximation is slightly more formidable. Overall, the isothermal approximation provides an adequate fit to the vertical structure of edge-on spirals (van der Kruit & Searle 1982) and the stellar kinematics of the solar neighborhood (e.g., Wielen 1977). However, near the galactic plane, the approximation breaks down: the stellar density distribution is more sharply peaked than the isothermal model would predict (Fuchs & Wielen 1987; de Grijs & van der Kruit 1996). This has led van der Kruit (1988) to consider a family of alternative models, which have isothermal ($\mathrm{sech}^2(z/z_0)$) and exponential ($\exp(-z/z_e)$) spatial distributions as their limiting cases. According to these models, M33's surface mass can be up to 33% larger than that derived using the simple isothermal assumption.

The final systematic uncertainty that is not included in Table 6 is one that affects our mass-to-light ratio measurements in M33's outer regions. Reliable optical and infrared surface photometry exist only for M33's inner $\sim 20'$; outside of this region, one must extrapolate the galaxy's surface brightness from its measured scale length. The length of this extrapolation is significant, so a small error in scale length propagates into a large error in M/L. Moreover, if M33's disk is truncated (e.g., Kregel, van der Kruit, & de Grijs 2002), or if a small amount of excess luminosity is left over from a tidal interaction, then the derived mass-to-light ratios will be seriously in error. In fact, the extrapolated $V - K$ color for the outer disk of M33 is not consistent of any population synthesis model (e.g., Maraston 1998). Given the uncertainties associated with infrared photometry, our anomalously large values for M/L_K in the outer disk of the galaxy are almost certainly due to errors in the extrapolated K-band surface photometry.

8. The Scale Length of M33's Disk

Our value for M33's disk scale length is more than twice that of the galaxy's infrared light, and 1.5 times that of the galaxy's V light. This discrepancy implies a gradient in the galaxy's disk mass-to-light ratio. Specifically, our observations imply that M33's disk M/L slowly increases with radius. Part of this increase is due to the growing contribution of M33's interstellar medium, which has a density distribution that is much flatter than that of the stars (Heyer et al. 2004). However, even when this component is taken into account, a positive gradient the disk mass-to-light ratio remains. The sign of this gradient runs contrary to

expectations: in most models of galaxy formation, it is the inner regions of a galaxy that form first, and contain the older, higher mass-to-light ratio stars (e.g., Eggen, Lynden-Bell, & Sandage 1962; Searle & Zinn 1978; Fall & Efstathiou 1980; Steinmetz & Müller 1994). Moreover, multi-color imaging (Bell & de Jong 2000) and Hα surface photometry (Ryder & Dopita 1994) tend to support this picture: most disks appear to possess significant age gradients that are consistent with the inside-out scenario. Thus, we must consider the possibility that our mass measurements are biased. In fact, there are several effects which could conceivably introduce a systematic error into our estimates of σ_z. If any of these exist, then our value for the galaxy's kinematic scale length could be in error.

The first possible bias comes from contamination by emission-line objects that are not planetary nebulae. In M33, H II regions and supernova remnants far outnumber planetary nebulae, and, as Population I objects, their velocity dispersions are significantly less than that of the PNe (e.g., Zaritsky, Elston, & Hill 1989). If the fraction of contaminants is higher near the center of M33 than it is at large radii, then a systematic error in the scale length will be the result. Some support for this hypothesis comes from the image quality of the [O III] $\lambda 5007$ frame of M33's central field: the seeing on that image ($1''05$) is the poorest of any frame in the Massey et al. (2002) survey.

Still, for all the reasons detailed in Section 2, contamination is unlikely to be a significant problem in our survey. All of our PN candidates were detected both in [O III] $\lambda 5007$ and in Hα, and the excellent seeing on the latter image (and on the broadband V frame) should have excluded virtually all H II regions from our sample. Similarly, given the survey's image quality, and the intrinsic ratio of PNe to supernovae, it is difficult to envision how the fraction of faint compact supernova remnants could be large enough to cause a systematic error in R_z. At worst, contamination should cause only a slightly underestimate in σ_z throughout the galaxy.

A second possible explanation for the large kinematic scale length involves a selection effect. The inner regions of M33 are quite dusty, with internal extinction values of $A_V \sim 1$ mag (Israel & Kennicutt 1980; Berkhuijsen 1983; Regan & Vogel 1994; Petersen & Gammelgaard 1997). Consequently, PN surveys in this area are biased against objects in, and on the far side of the galactic plane. Under the isothermal disk approximation, this bias is irrelevant, since the velocity dispersion of such a disk is independent of galactic latitude. However, high above the plane, where the stellar orbits reach turn-around, the approximation must break down. If most of the PNe in our sample are high latitude objects, then it is possible that our PN velocities are not representative of the true kinematic structure of the disk.

Since M33's internal extinction declines rapidly with radius (Israel & Kennicutt 1980; Berkhuijsen 1983; Regan & Vogel 1994; Petersen & Gammelgaard 1997), the above selection effect has the potential for creating an artificial gradient in σ_z. However, the effect goes in the wrong direction. If extinction is to produce an overestimate of the disk's kinematic scale length, the PNe at high galactic latitude must have a lower dispersion that those near the plane. Yet models developed to fit the luminosity profiles of edge-on galaxies all have vertical velocity dispersions that increase with galactic latitude (van der Kruit 1988). So while internal extinction may indeed be censoring our data, the effect cannot produce the observed discrepancy.

A third way of explaining our large value of R_z involves our basic assumptions about the kinematics of M33's disk and the stability criteria. As Figure 9 demonstrates, the PN velocities, by themselves, do not fix σ_z. Instead, it is the velocity dispersion measurements, in combination with the requirements of dynamic stability, that produce the galaxy's dispersion gradient. If our warped-disk model for M33 is incorrect, or if the stability criteria have an additional radial dependence, or if the isothermal approximation breaks down at large radii, then an error in the scale length could be the result.

The first of these possibilities can quickly be excluded: in the area covered by our survey, the effects of M33's warp are minimal. In fact, if we were to model the galaxy using a simple flat-disk geometry, the derived kinematic scale length of the system would *increase* by $\sim 10\%$.

The latter two uncertainties are more difficult to assess. Certainly, the stability criterion given by (11) is only an approximation, as it assumes spiral-arm pitch angles that are close to zero, and neglects (among other things) the thickness of the disk and the existence of gaseous sub-systems. Nevertheless, numerical experiments suggest that the formulation is approximately correct (e.g., Griv et al. 1999; Khoperskov, Zasov, & Tyurina 2003). Similarly, though the limit on σ_z/σ_R from the buckling (or fire-hose) instability is not precisely known, the numerical experiments to date all indicate that a dispersion ratio of ~ 0.3 is reasonable (Araki 1985; Merritt & Sellwood 1994; Sellwood 1996). Finally, though one expects the isothermal approximation to become less accurate at large radii (due to the longer timescales for stellar interactions), surface photometry of edge-on spirals suggests otherwise (e.g., van der Kruit & Searle 1982; Fry et al. 1999; Bizyaev & Mitronova 2002).

The final way of creating an artificial gradient in M33's disk mass-to-light ratio is through the introduction of a radial gradient in the PN scale height. Our measurement of the disk scale length assumes that z_0 is constant throughout the galaxy, and, for disks in general, this is a good assumption (e.g., Shaw & Gilmore 1990; de Grijs & van der Kruit 1996; de Grijs & Peletier 1997). However, our analysis also assumes that PNe belong to the thin disk system and that the PN scale height does not change with radius.

The former assumption is certainly valid. Although deep observations of edge-on galaxies often reveal the existence of red "thick disk" envelopes (e.g., Dalcanton & Bernstein 2002), the amount of luminosity in this component is small enough so that thick disk PNe should be exceedingly rare. PN surveys of the edge-on spirals NGC 891 (Ciardullo, Jacoby, & Harris 1991) and NGC 4565 (Jacoby, Ciardullo, & Harris 1996) confirm this fact: very few objects are found in the thick disk region. Still, within the thin disk, the scale height of PNe could still change. For example, in the solar neighborhood, the vertical velocity dispersion of a stellar population is roughly proportional to the square root of the population's age (e.g., Wielen 1977; Jahreiß & Wielen 1983). Since planetary nebulae are derived from a mix of populations with turnoff masses between $1M_\odot \lesssim M \lesssim 5M_\odot$, their dispersion is a weighted average over the age range which corresponds to these masses, i.e., from $t_1 \sim 10^{10}$ yr to $t_2 \sim 10^8$ yr. In other words,

$$\langle \sigma_z^2 \rangle = \int_{t_1}^{t_2} \Phi(t)\, \frac{dN}{dm_{tn}}\, \frac{dm_{tn}}{dt}\, \sigma_z^2(t)\, dt \tag{17}$$

where $\Phi(t)$ is the region's star formation rate history, and m_{tn} is the main-sequence turnoff mass of a population with age t. Since velocity dispersion is related to scale height via equation (6), this means that a gradient in a galaxy's star-formation rate history can produce an artificial gradient in the PN scale height.

Figure 11 quantifies this effect for the case where Φ declines exponentially with scale time τ. In late-type spirals such as M33, the evidence suggests that the rate of star formation has been roughly constant over a Hubble time (Kennicutt, Tamblyn, & Congdon 1994). If this is the case, then $\tau \gg 1$, and the dependence of σ_z on Φ is weak. Nevertheless, if the star-formation rate history of M33's inner disk is substantially different from that of its outer disk, a systematic error in our mass determinations may be the result.

Unfortunately, the effect shown in Figure 11 is much too small to explain M33's large kinematic scale length: in order to be consistent with a constant M/L_V disk, the scale height of M33's PNe would have to change by almost an order of magnitude, from $\gtrsim 500$ pc near the galactic center, to $\lesssim 100$ pc at 8 kpc. Not only is this many times greater than what can be achieved by changing the galaxy's star formation rate history, but the direction of the effect is wrong. If the stars of M33's interior are systematically older

than the stars of the outer disk (as might be expected from an inside-out galaxy formation scenario), then our assumption of a constant z_0 would produce an overestimate of the surface mass in the inner regions of the galaxy, and an underestimate of surface mass in the outer disk. This would cause us to underestimate the scale length of the system. Moreover, the discrepancy between the galaxy's photometric and dynamical scale lengths would be exacerbated by the reaction of the system's infrared light to such a gradient. While the K-band is far superior to the optical when in comes to viewing stellar luminosity through the veil of interstellar extinction, it is not immune from population effects. Just as the OB stars of present day star formation distort surface brightness measurements made in B, red supergiants left over from star-formation of the recent past contaminate data taken in K. Although photometric enhancements in the infrared are less than those in the optical, they are still substantial (Regan & Vogel 1994), and if the interior regions of M33 are older than the stars of the outer disk, the galaxy's IR luminosity profile will appear more diffuse that the mass. This is the opposite of what is seen.

We note that, in principle, the question of M33's star formation history can be answered via planetary nebula spectrophotometry. Kaler & Jacoby (1990) have shown that the ratio of nitrogen to oxygen in a planetary nebula correlates with its core mass: objects with $M_c < 0.65 M_\odot$ have N/O ~ 0.2, while higher mass objects have $1 \lesssim$ N/O $\lesssim 2$. Consequently, this discontinuity, which is most likely caused by dredge-up in AGB stars with $M \gtrsim 3M_\odot$ (Iben & Renzini 1983), can be used to identify the PNe of high mass progenitors. Furthermore, Dopita et al. (1997) have shown that one can estimate PN central star masses directly by using deep spectrophotometry to locate the stars on the HR diagram, and then comparing their locations to post-AGB evolutionary models. This technique, when combined with an initial-mass final-mass relation (i.e., Weidemann 2000), can allow us to trace the star-formation history of different parts of M33's disk, and test for the presence of age gradients in the PN sample.

9. M33's Disk and Halo

There have been numerous efforts to probe the radial distribution of M33's dark halo via the shape of the galaxy's rotation curve (e.g., Giraud 2000; Corbelli & Salucci 2000; Corbelli 2003). However, these efforts have all been limited by the unknown mass-to-light ratio of the galaxy's disk. The disk-mass estimates of Table 6 provide a new constraint on M33's mass distribution, and help break the disk-halo degeneracy.

To demonstrate this constraint, we began by fitting a smooth Brandt (1960) curve to the H I and CO rotation measurements of Corbelli (2003). We then used our mass model to infer a rotation curve of the disk alone. The radial profile of the dark halo was then estimated by simply differencing the two components. Figure 12 illustrates this disk-halo decomposition.

From the rotation curves of Figure 12 and the mass-to-light ratios of Table 6, it is clear that there is very little dark matter in M33's central regions. Based on our PN velocity dispersion measurements, the disk mass-to-light ratios for M33's central ~ 2 kpc are $M/L_K \sim 0.2$ and $M/L_V \sim 0.3$. Both these values are close to those predicted for stellar populations dominated by young ($\tau \sim 150$ Myr old) stars (Maraston 1998; Bell & de Jong 2001). More importantly, these numbers are statistically identical to those obtained using the galaxy's H I and CO rotation curve, and are also similar to the central mass-to-light ratios derived from the rotation curves of other spirals (e.g., Moriondo, Giovanardi, & Hunt 1998). This consistency implies that the constant mass-to-light approach of "maximal disk" models is tenable, at least in the inner regions of galaxies.

Outside of ~ 2 kpc, M33's disk mass-to-light ratio exhibits a small, but distinct gradient, going from

$M/L_V \sim 0.3$ at ~ 2 kpc to $M/L_V \sim 1.5$ at ~ 8.5 kpc. Since this appears to be in conflict with the inside-out model of galaxy formation, one possible explanation is the presence of dark matter associated with M33's disk. Indeed, M33's disk-mass alone produces a rotation curve that is more-or-less flat with radius.

Another explanation is the increasing importance of M33's gaseous disk. The surface density of M33's gas declines more slowly than that of galaxy's optical light (Regan & Vogel 1994; Corbelli 2003). Consequently, at large radii, this component can be expected to dominate the disk's mass budget. However, as summarized in Table 6, the radius where this occurs lies significantly outside the region of our survey. Even in our outermost bin, M33's interstellar medium comprises only $\sim 25\%$ of the disk mass.

One final explanation for the behavior of M33's disk mass-to-light ratio lies in the vigorous star formation occurring in M33's inner regions. It is entirely possible that, near the center of the galaxy, the mass contributed by the region's older, higher mass-to-light ratio populations is being overwhelmed by the luminosity of present-day stars. Evidence for this possibility comes from the results of Corbelli (2003) and Heyer et al. (2004), who demonstrate that star formation rate of M33's disk has a steeper radial dependence than the galaxy's V-light.

Whatever the reason for M33's increasing disk mass-to-light ratio, the fact that the galaxy's disk mass-to-light ratios are consistent with those expected from young stellar populations strongly suggests that dark matter is not an important constituent of the disk. Models, such as the molecular gas hypothesis of Pfenniger, Combes, & Martinet (1994), are certainly ruled out.

Our analysis is based on the velocities of only 140 PNe, so the spatial resolution of our measurements is poor. However, if we assume that M33's disk has an exponential profile, and that our surface mass densities are accurate, then we can use our disk/halo decomposition to place limits on the radial profile of the galaxy's dark matter. According to Cold Dark Matter models of galaxy formation, systems such as M33 should contain "cusps" of dark matter at their center, with power-law density profiles in the range $-1 > \alpha > -1.5$, where $\rho_h \propto r^\alpha$ (e.g., Navarro, Frenk, & White 1996; Moore et al. 1998; Davé et al. 2001; Klypin et al. 2001; Power et al. 2003). As is illustrated in the lower panel of Figure 12, our central slope is much shallower than this, with $\alpha \gtrsim -0.5$. This result is robust: if we alter the PN scale height by 50%, or change the disk scale length by 25%, or increase the total disk mass 33% (either by adopting an exponential law for the disk's vertical profile, or by changing the central value of σ_z), the slope of M33's dark matter core remains low. The result also agrees with the conclusions of Corbelli (2003), who ruled out the presence of a steep dark matter core in M33 on the basis of the galaxy's rotation curve, and the assumption of a constant (K-band) mass-to-light ratio disk. Our analysis removes the latter assumption, but is otherwise similar.

If our analysis is correct, then M33 is another example of a galaxy whose interior dark matter profile is flat. High resolution rotation curves now exist for a large number of low-luminosity and low-surface brightness spirals and dwarfs, and every one is consistent with a value of $\alpha > -1$ (e.g., Borriello & Salucci 2001; Swaters et al. 2003). It is still unclear whether this shallow a slope is a critical problem for the Cold Dark Matter paradigm (de Blok, Bosma, & McGaugh 2003), or whether the discrepancy can be explained by the limitations in the measurements or the models (Swaters et al. 2003; Spekkens, & Giovanelli 2003). Nevertheless, M33 appears to be another example this problem.

Outside of ~ 1 kpc, our analysis suggests that M33's dark matter halo obeys the inverse-square law density dependence that is expected from isothermal and Navarro, Frenk, & White (1996) distributions. Because the dynamical scale length of the disk is larger than the photometric scale length, the system's total disk mass is larger than that expected from the maximal disk hypothesis. Within a radius of 10 kpc, our velocity dispersion measurements yield a disk mass $\sim 9.1 \times 10^9 M_\odot$. This is ~ 2.5 times larger than one

would obtain using V-band surface photometry and the maximum disk hypothesis, and ~ 6 times larger than one would derive from a similar analysis in K. Still, within this radius, M33's disk contains only $\sim 30\%$ of the total mass of the galaxy.

Of course, M33's disk does not end at 10 kpc. Although our planetary nebula detections end near this 10 kpc limit, observations of M33's H I gas extend to nearly twice that distance (Corbelli 2003). The interpretation of the extended H I data is made slightly more difficult by the increasing importance of the galactic warp at large radii. Nevertheless, if the models of Corbelli & Schneider (1997) and Corbelli & Salucci (2000) are accurate, then M33's rotational velocity increases from ~ 110 km s^{-1} to ~ 135 km s^{-1} between 10 kpc and 20 kpc. This suggests that the bulk of M33's dark matter halo still resides outside the region of our survey.

10. Conclusions

Until now, our knowledge of the stellar kinematics of spiral galaxies has come principally from observations of stars in the solar neighborhood, and secondarily from absorption-line measurements in the inner regions of face-on and edge-on spirals. Our planetary nebula observations have improved upon this situation. For the first time, we have been able to measure the shape of the stellar velocity ellipsoid throughout a galactic disk, and directly measure the variation in a galaxy's disk mass surface density. Our data suggest that, in the inner regions of galaxies, maximal disk models for the rotation curve are appropriate, and the contribution of dark matter is negligible. However, the data also show that the mass-to-light ratios of galactic disks do change with radius, and the M/L of the inner disk may be a factor of $\gtrsim 4$ smaller than that of the outer disk. Still, the existence of this gradient does not change the fact that most of a galaxy's material lies well away from the disk in a dark halo that roughly follows an inverse square density law. Models in which the dark matter is in the form of molecular gas are excluded by our observations.

REFERENCES

Araki, S. 1985, Ph.D. thesis, Massachusetts Institute of Technology

Ashman, K.M. 1992, PASP, 104, 1109

Bell, E.F., & de Jong, R.S. 2000, ApJ, 312, 497

Bell, E.F., & de Jong, R.S. 2001, ApJ, 550, 212

Berkhuijsen, E.M. 1983, A&A, 127, 395

Bevington, P.R. 1969, Data Reduction and Error Analysis for the Physical Sciences (New York: McGraw-Hill)

Bienaymé, O. 1999, A&A, 341, 86

Binney, J., & Tremaine, S. 1987, Galactic Dynamics, (Princeton: Princeton Univ. Press)

Bizyaev, D., & Mitronova, S. 2002, A&A, 389, 795

Borriello, A., & Salucci, P. 2001, MNRAS, 323, 285

Bothun, G.D. 1992, AJ, 103, 104

Bottema, R. 1993, A&A, 275, 16

Bottema, R., van der Kruit, P.C., & Freeman, K.C. 1987, A&A, 178, 77

Brandt, J.C. 1960, ApJ, 131, 293

Brandt, J.C. 1965, MNRAS, 129, 309

Cardelli, J.A., Clayton, G.C., & Mathis, J.S. 1989, ApJ, 345, 245

Carlberg, R.G. 1987, ApJ, 322, 59

Chen, B., Stoughton, C., Smith, J.A., Uomoto, A., Pier, J.R., Yanny, B., Ivezíc, Ž, York, D.G., Anderson, J.E., Annis, J., Brinkmann, J., Csabai, I., Fukugita, M., Hindsley, R., Lupton, R., & Munn, J.A. 2001, ApJ, 553, 184

Ciardullo, R. 2003 in Lecture Notes in Physics: Stellar Candles for the Extragalactic Distance Scale, ed. W. Gieren & D. Alloin (Heidelberg: Springer-Verlag), 243

Ciardullo, R., Ford, H.C., Neill, J.D., Jacoby, G.H., & Shafter, A.W. 1987, ApJ, 318, 520

Ciardullo, R., Feldmeier, J.J., Jacoby, G.H., de Naray, R.K., Laychak, M.B., & Durrell, P.R. 2002, ApJ, 577, 31

Ciardullo, R., & Jacoby, G.H. 1999, ApJ, 515, 191

Ciardullo, R., Jacoby, G.H., Ford, H.C., & Neill, J.D. 1989, ApJ, 339, 53

Ciardullo, R., Jacoby, G.H., & Harris, W.E. 1991, ApJ, 383, 487

Combes, F. 2002, New Astronomy Reviews, 46, 755

Corbelli, E. 2003, MNRAS, 342, 199

Corbelli, E., & Salucci, P. 2000, MNRAS, 311, 441

Corbelli, E., & Schneider, S.E. 1997, ApJ, 479, 244

Corradi, R.L.M., & Schwarz, H.E. 1995, A&A, 293, 871

Dalcanton, J.J., & Bernstein, R.A. 2002, AJ, 124, 1328

Davé, R., Spergel, D.N., Steinhardt, P.J., & Wandelt, B.D. 2001, ApJ, 547, 574

de Blok, W.J.G., Bosma, A., & McGaugh, S. 2003, MNRAS, 340, 657

de Grijs, R., & Peletier, R.F. 1997, A&A, 320, L21

de Grijs, R., & van der Kruit, P.C. 1996, A&AS, 117, 19

de Vaucouleurs, G. 1959, ApJ, 130, 728

de Vaucouleurs, G., de Vaucouleurs, A., Corwin, H.G. Jr., Buta, R.J., Paturel, G., & Fouqué, P. 1991, Third
    Reference Catalog of Bright Galaxies, (New York: Springer-Verlag)

Dehnen, W., & Binney, J.J. 1998, MNRAS, 298, 387

Dopita, M.A., Jacoby, G.H., & Vassiliadis, E. 1992, ApJ, 389, 27

Dopita, M.A., Vassiliadis, E., Wood, P.R., Meatheringham, S.J., Harrington, J.P., Bohlin, R.C., Ford, H.C.,
    Stecher, T.P., & Maran, S.P. 1997, ApJ, 474, 188

Eggen, O.J., Lynden-Bell, D., & Sandage, A.R. 1962, ApJ, 136, 748

Faber, S.M., & Gallagher, J.S. 1979, ARA&A, 17, 135

Fall, S.M., & Efstathiou, G. 1980, MNRAS, 193, 189

Freedman, W.L., Madore, B.F., Gibson, B.K., Ferrarese, L., Kelson, D.D., Sakai, S., Mould, J.R., Kennicutt,
    R.C. Jr., Ford, H.C., Graham, J.A., Huchra, J.P., Hughes, S.M.G., Illingworth, G.D., Macri, L.M., &
    Stetson, P.B. 2001, ApJ, 553, 47

Freedman, W.L., Wilson, C.D., & Madore, B.F. 1991, ApJ, 372, 455

Fry, A.M., Morrison, H.L., Harding, P., & Boroson, T.A. 1999, AJ, 118, 1209

Fuchs, B., & Wielen, R. 1987, in NATO ASIC Proc. 207, The Galaxy, ed. G. Gilmore & B. Carswell
    (Dordrecht: Reidel), 375

Garnett, D.R., Shields, G.A., Skillman, E.D., Sagan, S.P., & Dufour, R.J. 1997, ApJ, 489, 63

Gebhardt, K., Lauer, T.R., Kormendy, J., Pinkney, J., Bower, G.A., Green, R., Gull, T., Hutchings, J.B.,
    Kaiser, M.E., Nelson, C.H., Richstone, D., & Weistrop, D. 2001, AJ, 122, 2469

Gerssen, J., Kuijken, K., & Merrifield, M.R. 1997, MNRAS, 288, 618

Gerssen, J., Kuijken, K., & Merrifield, M.R. 2000, MNRAS, 317, 545

Giraud, E. 2000, ApJ, 539, 155

Griv, E., Rosenstein, B., Gedalin, M., & Eichler, D. 1999, A&A, 347, 821

Guidoni, U., Messi, R., & Natali, G. 1981, A&A, 96, 215

Henize, K.G., & Westerlund, B.E. 1963, ApJ, 137, 747

Heyer, M.H., Corbelli, E., Schneider, S.E., & Young, J.S. 2004, ApJ, 602, 723

Hippelein, H., Haas, M., Tuffs, R.J., Lemke, D., Stickel, M., Klaas, U., & Völk, H.J. 2003, A&A, 407, 137

Hodge, P.W., Balsley, J., Wyder, T.K., & Skelton, B.P. 1999, PASP, 111, 685

Huchra, J.P., Vogeley, M.S., & Geller, M.J. 1999, ApJS, 121, 287

Hui, X., Ford, H.C., Ciardullo, R., & Jacoby, G.H. 1993, ApJ, 414, 463

Iben, I., Jr., & Laughlin, G. 1989, ApJ, 341, 312

Iben, I., Jr., & Renzini, A. 1983, ARA&A, 21, 271

Israel, F.P., & Kennicutt, R.C. 1980, Astrophys. Lett., 21, 1

Jacoby, G.H. 1989, ApJ, 339, 39

Jacoby, G.H. 1997, in The Extragalactic Distance Scale, Space Telescope Science Institute Series, ed. M. Livio (Cambridge: Cambridge University Press), 197

Jacoby, G.H., Branch, D., Ciardullo, R., Davies, R.L., Harris, W.E., Pierce, M.J., Pritchet, C.J., Tonry, J.L., & Welch, D.L. 1992, PASP, 104, 599

Jacoby, G.H., Ciardullo, R., Ford, H.C., & Booth, J. 1989, ApJ, 344, 70

Jacoby, G.H., Ciardullo, R., & Harris, W.E. 1996, ApJ, 462, 1

Jacoby, G.H., & De Marco, O. 2002, AJ, 123, 269

Jacoby, G.H., Quigley, R.J., & Africano, J.L. 1987, PASP, 99, 672

Jahreiß, H., & Wielen, R. 1983, IAU Colloq. 76, Nearby Stars and the Stellar Luminosity Function, ed. A.G.D. Philip & A.R. Upgren (Schenectady: L. Davis Press), 277

Jenkins, A., & Binney, J. 1990, MNRAS, 245, 305

Kaler, J.B., & Jacoby, G.H. 1990, ApJ, 362, 491

Kennicutt, R.C., Tamblyn, P., & Congdon, C.E. 1994, ApJ, 435, 22

Kent, S.M. 1986, AJ, 91, 1301

Kent, S.M. 1987, AJ, 94, 306

Khoperskov, A.V., Zasov, A.V., & Tyurina, N.V. 2003, Astronomy Reports, 47, 357

Kim, M., Kim, E., Lee, M.G., Sarajedini, A., & Geisler, D. 2002, AJ, 123, 244

Klypin, A., Kravtsov, A.V., Bullock, J.S., & Primack, J.R. 2001, ApJ, 554, 903

Kregel, M., van der Kruit, P.C., & de Grijs, R. 2002, MNRAS, 334, 646

Kurtz, M.J., & Mink, D.J. 1998, PASP, 110, 934

Maciel, W.J. 1989, in IAU Symp. 131, Planetary Nebulae, ed. S. Torres-Peimbert (Dordrecht: Kluwer), 73

Magrini, L., Cardwell, A., Corradi, R.L.M., Mampaso, A., & Perinotto, M. 2001, A&A, 367, 498

Magrini, L., Corradi, R.L.M., Mampaso, A., & Perinotto, M. 2000, A&A, 355, 713

Magrini, L., Perinotto, M., Corradi, R.L.M., & Mampaso, A. 2003, A&A, 400, 511

Maraston, C. 1998, MNRAS, 300, 872

Marigo, P., Girardi, L., Weiss, A., Groenewegen, M.A.T., & Chiosi, C. 2004, A&A, in press

Massey, P., Bianchi, L., Hutchings, J.B., & Stecher, T.P. 1996, ApJ, 469, 629

Massey, P., Hodge, P.W., Holmes, S., Jacoby, J., King, N.L., Olsen, K., Smith, C., & Saha, A. 2002, BAAS, 34, 1272

Merritt, D., & Sellwood, J.A. 1994, ApJ, 425, 567

Mihalas, D., & Binney, J. 1981 Galactic Astronomy (New York: Freeman)

Monet, D., Bird, A., Canzian, B., Dahn, C., Guetter, H., Harris, H., Henden, A., Levine, S., Luginbuhl, C., Monet, A.K.B., Rhodes, A., Riepe, B., Sell, S., Stone, R., Vrba, F., & Walker, R. 1998, PMM USNO-A2.0: A Catalogue of Astrometric Standards (Washington, DC: US Naval Obs.)

Moore, B., Governato, F., Quinn, T., Stadel, J., & Lake, G. 1998, ApJ, 499, L5

Moriondo, G., Giovanardi, C., & Hunt, L.K. 1998, A&A, 339, 409

Morozov, A.G. 1980, SvA, 24, 391

Morozov, A.G. 1980, SvA, 25, 19

Morozov, A.G. 1980, SvA, 25, 421

Navarro, J.F., Frenk, C.S., & White, S.D.M. 1996, ApJ, 462, 563

Palunas, P., & Williams, T.B. 2000, AJ, 120, 2884

Peimbert, M. 1993, in IAU Symp. 155, Planetary Nebulae, ed. R. Weinberger & A. Acker (Dordrecht: Kluwer), 523

Petersen, L., & Gammelgaard, P. 1997, A&A, 323, 697

Pfenniger, D., Combes, F., & Martinet, L. 1994, A&A, 285, 79

Phillips, J.P. 2003, New Astronomy, 8, 29

Pottasch, S.R. 1984, Planetary Nebulae, (Dordrecht: Reidel), Chapter 5

Power, C., Navarro, J.F., Jenkins, A., Frenk, C.S., White, S.D.M., Springel, V., Stadel, J., & Quinn, T. 2003, MNRAS, 338, 14

Ratnatunga, K.U., & Upgren, A.R. 1997, ApJ, 476, 811

Regan, M.W., & Vogel, S.N. 1994, ApJ, 434, 536

Rogstad, D.H., Wright, M.C.H., & Lockhart, I.A. 1976, ApJ, 204, 703

Rubin, V. 1997, Bright Galaxies, Dark Matters, (Woodbury, NY: American Institute of Physics)

Ryder, S.D., & Dopita, M.A. 1994, ApJ, 430, 142

Sandage, A., & Humphreys, R.M. 1980, ApJ, 263, L1

Scalo, J.M. 1986, FCPh, 11, 1

Schlegel, D.J., Finkbeiner, D.P., & Davis, M. 1998, ApJ, 500, 525

Schwarzkopf, U., & Dettmar, R.-J. 2001, A&A, 373, 402

Searle, L., & Zinn, R. 1978, ApJ, 225, 357

Sellwood, J.A. 1996, ApJ, 473, 733

Shaver, P.A., McGee, R.X., Newton, L.M., Danks, A.C., & Pottasch, S.R. 1983, MNRAS, 204, 53

Shaw, M.A., & Gilmore, G. 1990, MNRAS, 242, 59

Sofue, Y., Koda, J., Nakanishi, H., & Onodera, S. 2003, PASJ, 55, 59,

Spekkens, K., & Giovanelli, R. 2003, in IAU Symp. 220, Dark Matter in Galaxies, ed. S. Ryder, D.J. Pisano, M. Walker, & K. Freeman (San Francisco: ASP), in press

Steinmetz, M., & Müller, E. 1994, A&A, 281, 97

Stetson, P.B. 1987, PASP, 99, 191

Stetson, P.B. 1992, in ASP Conf. Ser. 25, Astronomical Data Analysis Software and Systems I., ed. D.M. Worral, C. Biemesderfer, & J. Barnes (San Francisco: ASP), 297

Stetson, P.B., Davis, L.E., & Crabtree, D.R. 1990, in ASP Conf. Ser. 8, CCDs in Astronomy, ed. G.H. Jacoby (San Francisco: ASP), 289

Stone, R.P.S. 1977, ApJ, 218, 767

Swaters, R.A., Madore, B.F., van den Bosch, F.C., & Balcells, M. 2003, ApJ, 583, 732

Tiede, G.P., Sarajedini, A., & Barker, M.K. 2004, AJ, in press

Toomre, A. 1964, ApJ, 139, 1217

Toomre, A. 1966, in Notes on the 1966 Summer Study Program in Geophysical Fluid Dynamics at the Woods Hole Oceanographic Institution (Woods Hole: Woods Hole Oceanographic Institute), 111

Udalski, A., Szymański, M., Kubiak, M., Pietrzyński, G., Soszyński, I., Woźniak, P., & Żebruń, K. 1999, Act. Astr., 49, 201

Valdes, F.G. 1998, in ASP Conf. Ser. 145, Astronomical Data Analysis Software and Systems VII, ed. R. Albrecht, R.N. Hook, & H.A. Bushhouse (San Francisco: ASP), 53

van der Kruit, P.C. 1988, A&A, 192, 117

van der Kruit, P.C., & de Grijs, R. 1999, A&A, 352, 129

van der Kruit, P.C., & Searle, L. 1982, A&A, 110, 61

van der Kruit, P.C., Jiménez-Vicente, J., Kregel, M., & Freeman, K.C. 2001, A&A, 379, 374

Vassiliadis, E., & Wood, P.R. 1994, ApJS, 92, 125

Villumsen, J.V. 1985, ApJ, 290, 75

Weidemann, V. 2000, A&A, 363, 647

Wielen, R. 1977, A&A, 60, 263

Zaritsky, D., Elston, R., & Hill, J.M. 1989, AJ, 97, 97

Zijlstra, A.A., & Pottasch, S.R. 1991, A&A, 243, 478

Table 1.   M33 Survey

Field	α(2000)	δ(2000)	Filter	Bandpass	Number of Exposures	Total Exp Time (min)	Seeing
M33 Center	1:33:49.0	+30:40:00	[O III]	55 Å	5	25	1″05
M33 Center	1:33:49.0	+30:40:00	Hα	80 Å	5	25	0″90
M33 Center	1:33:49.0	+30:40:00	V	940 Å	5	1	0″95
M33 Center	1:33:49.0	+30:40:00	B	990 Å	5	1	0″95
M33 North	1:34:00.0	+30:55:37	[O III]	55 Å	5	25	0″90
M33 North	1:34:00.0	+30:55:37	Hα	80 Å	5	25	0″70
M33 North	1:34:00.0	+30:55:37	V	940 Å	5	1	1″05
M33 North	1:34:00.0	+30:55:37	B	990 Å	5	1	1″05
M33 South	1:33:10.5	+30:22:30	[O III]	55 Å	5	25	0″95
M33 South	1:33:10.5	+30:22:30	Hα	80 Å	5	25	0″75
M33 South	1:33:10.5	+30:22:30	V	940 Å	5	1	0″85
M33 South	1:33:10.5	+30:22:30	B	990 Å	5	1	0″85

Table 2.   M33 Planetary Nebula Candidates

ID	$\alpha(2000)$	$\delta(2000)$	m_{5007}	$n_p{}^a$	$\log(F_{H\alpha})^b$	$\frac{F(\text{[O III]})}{F(\text{H}\alpha)}$	err	$n_s{}^c$	$v_\odot$	σ_v	M01^d	Notes
1	1:32:09.04	30:22:05.7	23.51	1	−15.321	2.628	0.176	2	−139.2	3.6		
2	1:32:26.54	30:25:49.8	23.53	2	−15.390	3.042	0.204	2	−127.7	1.9	1	O
3	1:32:38.03	30:24:00.6	21.82	2	−14.243	1.046	0.019	2	−130.3	1.6	2	O
4	1:32:39.80	30:37:41.0	22.07	2	−14.602	1.891	0.047	3	−208.4	1.7	3	
5	1:32:40.08	30:35:15.3	23.38	2	−15.343	3.125	0.154	2	−160.4	2.7		
6	1:32:42.72	30:12:25.5	22.63	1	−14.895	2.218	0.085	2	−106.7	2.0	4	
7	1:32:44.29	30:43:25.9	24.74	2	−15.655	1.837	0.153	3	−185.9	3.0	6	
8	1:32:49.16	30:51:09.1	21.45	2	−14.526	2.826	0.042	3	−192.2	2.0	7	
9	1:32:52.96	30:41:57.7	22.49	2	−14.778	1.930	0.041	2	−167.3	3.0	9	
10	1:32:53.72	30:32:25.8	23.73	2	−14.720	0.541	0.023	3	−136.3	5.4	12	O
11	1:32:55.04	30:09:52.9	21.34	1	−14.437	2.549	0.048	2	−88.5	1.1	13	
12	1:32:55.11	30:14:01.5	22.23	1	−14.859	2.948	0.090	2	−121.1	3.0		
13	1:32:58.80	30:27:38.0	22.28	2	−14.887	3.009	0.089	2	−136.0	1.8	14	
14	1:32:59.40	30:10:24.0	22.84	1	−14.459	0.671	0.019	2	−94.5	5.6	15	
15	1:33:01.25	30:15:31.1	23.42	1	−15.210	2.212	0.171	2	−114.7	3.6	16	O
16	1:33:05.62	30:42:15.1	23.43	2	−15.323	2.863	0.132	0	−136.6	8.4		O
17	1:33:05.86	30:50:44.2	23.48	2	−15.574	4.848	0.239	3	−201.8	2.9		
18	1:33:06.11	30:31:04.5	20.72	2	−14.289	3.203	0.050	3	−145.1	2.0	18	O
19	1:33:06.20	31:00:56.1	24.14	1	−15.823	4.669	0.513	4	−195.5	4.4		
20	1:33:07.44	30:54:23.2	21.14	2	−14.396	2.769	0.038	5	−187.1	2.3	17	
21	1:33:08.55	30:34:38.5	23.96	2	−15.705	4.211	0.526	2	−145.1	5.1		
22	1:33:08.99	30:13:58.6	23.78	1	−15.304	1.973	0.205	2	−91.1	3.7	19	O
23	1:33:11.96	30:30:48.2	22.74	2	−14.954	2.301	0.095	3	−156.8	1.3		
24	1:33:14.12	30:40:42.7	21.68	2	−14.630	2.897	0.065	5	−188.3	2.9	22	
25	1:33:15.50	30:17:53.7	24.51	1	−15.594	1.972	0.236	1	−133.0	12.8	25	
26	1:33:16.89	30:29:59.9	22.81	2	−14.928	2.025	0.060	3	−119.0	1.5	26	
27	1:33:17.01	30:29:59.8	24.53	1	−15.848	3.464	0.536	1	−120.6	7.2	29	
28	1:33:18.48	30:12:38.8	23.23	1	−15.276	3.076	0.174	2	−110.6	2.8	27	
29	1:33:19.25	30:29:40.2	20.93	2	−14.417	3.522	0.057	2	−141.1	1.4	28	
30	1:33:19.73	30:43:05.5	22.19	2	−14.476	1.273	0.023	3	−108.7	1.5	35	H, O
31	1:33:21.16	31:06:44.0	22.83	1	−15.104	3.006	0.113	2	−231.1	2.5	30	O
32	1:33:21.18	30:41:14.6	21.78	2	−14.534	2.116	0.051	2	−216.5	1.4	31	
33	1:33:21.59	30:36:57.2	23.22	2	−14.760	0.944	0.032	2	−112.8	7.0	32	
34	1:33:22.85	30:13:41.0	22.59	1	−14.791	1.823	0.067	2	−134.9	4.2	33	
35	1:33:23.65	30:19:39.8	23.59	1	−15.419	3.076	0.223	3	−120.1	4.9		
36	1:33:24.23	30:16:14.5	23.65	1	−15.214	1.813	0.141	3	−90.2	1.6	36	
37	1:33:25.11	30:45:06.2	24.45	2	−14.523	0.176	0.013	4	−192.4	8.8	130	
38	1:33:26.33	30:41:45.2	22.36	2	−14.490	1.118	0.024	2	−153.3	3.4	41	
39	1:33:26.59	30:35:50.3	22.41	2	−14.308	0.705	0.019	4	−135.4	7.6	38	
40	1:33:27.29	30:40:51.3	22.79	2	−14.390	0.598	0.014	2	−163.1	6.2	37	O
41	1:33:27.79	30:34:29.2	22.65	2	−14.442	0.771	0.020	3	−120.2	9.3	40	
42	1:33:27.89	31:06:22.3	25.45	1	−15.899	1.673	0.236	3	$\cdots$			O
43	1:33:28.50	30:37:45.8	22.24	2	−14.901	3.239	0.098	2	−120.8	1.1	39	
44	1:33:31.25	30:40:04.9	24.11	2	−15.767	4.238	0.698	0				NT
45	1:33:31.88	30:30:32.6	22.53	2	−14.604	1.245	0.035	3	−155.9	1.6	45	
46	1:33:32.17	30:28:20.2	20.95	2	−14.247	2.344	0.030	2	−123.8	2.4	42	
47	1:33:32.21	30:31:46.1	23.22	2	−14.564	0.603	0.032	2	−170.6	8.0		
48	1:33:32.34	30:42:40.4	21.89	2	−14.607	2.264	0.063	2	−229.4	2.4	49	
49	1:33:32.69	30:26:42.3	22.53	2	−14.409	0.794	0.019	3	−93.7	7.2	43	
50	1:33:33.15	30:37:34.4	22.15	2	−14.235	0.759	0.015	3	−144.3	6.0		
51	1:33:36.79	30:31:40.5	22.91	2	−15.218	3.611	0.205	2	−115.9	3.0	48	
52	1:33:36.83	30:38:45.6	23.68	3	−15.160	1.549	0.096	1	−146.9	7.0		
53	1:33:37.00	30:26:33.1	21.19	2	−14.309	2.170	0.031	2	−117.4	1.7	46	
54	1:33:38.56	30:33:02.3	22.50	2	−14.736	1.738	0.047	3	−107.5	2.3	51	
55	1:33:40.16	30:37:49.5	21.81	3	−14.572	2.249	0.040	1	−165.2	0.6		

Table 2—Continued

ID	α(2000)	δ(2000)	m_{5007}	n_p[a]	$\log(F_{H\alpha})$[b]	$\frac{F([\text{O III}])}{F(\text{H}\alpha)}$	err	n_s[c]	$v_\odot$	σ_v	M01[d]	Notes
56	1:33:42.30	30:37:39.7	21.70	2	-14.433	1.813	0.049	2	-171.0	2.0	54	
57	1:33:42.76	30:49:05.6	23.21	2	-14.802	1.053	0.035	5	-222.7	5.0	58	O
58	1:33:43.48	30:59:41.1	24.42	1	-14.583	0.209	0.012	3	-254.6	10.1	57	
59	1:33:43.75	30:33:26.6	22.67	2	-14.920	2.257	0.085	2	-122.7	4.7		
60	1:33:44.38	30:20:23.7	21.15	1	-14.409	2.844	0.060	2	-115.7	1.6	59	
61	1:33:44.62	31:04:03.5	25.21	1	-15.886	2.023	0.225	2	$\cdots$			O
62	1:33:45.12	31:08:33.5	25.54	1	-16.032	2.085	0.342	3	$\cdots$			O
63	1:33:45.62	30:25:56.3	23.54	2	-15.389	3.001	0.179	0	$\cdots$			O
64	1:33:46.09	30:33:35.8	23.11	2	-14.854	1.307	0.074	1	-106.4	4.7		
65	1:33:46.45	30:26:55.4	22.40	2	-14.884	2.682	0.079	3	-140.1	3.0	60	
66	1:33:46.73	30:17:33.5	21.15	1	-14.426	2.940	0.069	2	-107.1	2.2	61	
67	1:33:48.27	30:33:15.7	22.05	2	-14.412	1.246	0.028	1	-136.2	7.9		
68	1:33:48.57	30:35:47.9	21.65	2	-14.548	2.475	0.055	1	-95.5	1.7	62	
69	1:33:49.36	30:32:28.4	24.23	2	-14.381	0.156	0.009	1	-119.5	7.8		
70	1:33:49.41	30:32:06.6	21.73	2	-14.718	3.398	0.088	2	-159.5	2.9	65	
71	1:33:50.02	30:14:25.2	21.25	1	-14.444	2.818	0.056	2	-103.2	4.0	63	
72	1:33:50.82	30:18:43.8	23.90	1	-14.815	0.575	0.029	3	-93.2	6.2	64	
73	1:33:51.06	30:45:38.8	21.28	2	-14.361	2.247	0.050	3	-253.2	2.1	95	
74	1:33:52.05	30:48:56.3	23.63	1	-14.927	0.954	0.072	0	$\cdots$			O
75	1:33:52.64	30:16:54.2	21.05	1	-14.340	2.642	0.045	2	-112.4	4.7	67	
76	1:33:52.77	30:37:38.9	20.78	2	-14.279	2.948	0.045	2	-157.4	1.0	68	O
77	1:33:52.78	30:44:32.7	24.04	2	-15.304	1.556	0.171	3	-229.6	3.4	88	
78	1:33:54.68	30:36:05.7	21.59	2	-14.206	1.186	0.019	1	-147.4	6.0	69	
79	1:33:54.93	30:47:13.4	23.42	2	-15.170	2.023	0.141	2	-240.6	1.7		
80	1:33:55.58	30:16:02.9	23.94	1	-14.933	0.728	0.033	1	-97.2	8.0	71	O
81	1:33:56.22	30:41:57.0	23.60	2	-15.057	1.324	0.084	1	-157.1	3.4		H, O
82	1:33:56.97	30:54:12.5	21.21	2	-14.451	2.970	0.053	1	-260.8	2.2	72	
83	1:33:57.18	30:36:47.6	22.09	2	-14.871	3.471	0.096	1	-134.7	1.9	73	
84	1:33:57.55	30:42:50.0	23.05	2	-15.145	2.679	0.125	2	-230.6	1.5		
85	1:33:58.38	30:55:05.2	22.91	2	-14.812	1.415	0.072	1	-247.5	3.6		
86	1:33:59.97	30:40:28.7	21.62	2	-14.627	3.039	0.096	2	-212.8	2.0	74	
87	1:34:00.93	30:37:08.1	22.93	2	-15.668	9.972	1.821	1	-156.4	1.4		
88	1:34:01.12	30:50:27.3	20.95	2	-14.270	2.484	0.031	2	-248.1	2.4	75	O
89	1:34:02.04	30:50:41.3	23.37	2	-14.741	0.788	0.025	3	-253.6	7.9	76	
90	1:34:02.57	30:40:00.5	22.04	3	-14.782	2.959	0.069	2	-188.3	0.6	84	
91	1:34:02.61	30:23:25.5	24.24	2	-15.551	2.278	0.203	2	-161.2	7.5	77	
92	1:34:02.77	30:38:33.3	21.29	3	-14.328	2.064	0.065	1	-192.3	0.8		O
93	1:34:03.05	30:38:13.4	23.54	3	-15.014	1.266	0.060	2	-190.8	4.3		
94	1:34:03.54	30:39:15.6	21.25	3	-14.465	2.930	0.050	2	-169.6	2.5	79	O
95	1:34:03.64	30:52:39.7	22.52	2	-14.910	2.544	0.078	2	-258.6	0.7	80	
96	1:34:03.65	30:45:58.9	23.20	2	-14.484	0.508	0.019	2	-205.8	5.6	113	
97	1:34:05.54	31:12:30.1	25.17	1	-15.752	1.549	0.232	2	$\cdots$			
98	1:34:05.82	30:36:13.9	24.14	2	-15.111	0.910	0.072	1	-149.9	8.8		
99	1:34:06.56	30:48:23.3	22.05	2	-14.724	2.563	0.051	3	-263.2	1.3	83	
100	1:34:06.76	31:00:29.3	23.66	1	-15.246	1.941	0.130	2	-279.8	2.9	81	
101	1:34:08.65	30:43:33.5	23.16	2	-14.495	0.544	0.025	3	-213.7	5.6	106	
102	1:34:09.07	30:49:07.6	23.71	2	-14.784	0.639	0.035	2	-239.5	6.5	85	
103	1:34:09.57	30:36:24.8	22.32	2	-14.720	1.966	0.056	2	-173.5	2.2		
104	1:34:11.74	31:07:31.4	22.84	1	-14.431	0.627	0.023	1	-223.9	7.0	86	
105	1:34:11.91	30:45:00.9	21.32	2	-14.522	3.145	0.054	1	-235.0	2.1	119	
106	1:34:12.15	30:28:57.1	23.86	2	-14.848	0.641	0.030	0	-101.6	11.3		O
107	1:34:13.34	30:45:01.2	21.00	2	-14.403	3.227	0.052	1	-241.9	1.8	111	
108	1:34:13.40	30:33:50.7	21.21	2	-14.458	3.006	0.046	2	-115.9	1.5		O
109	1:34:13.98	30:22:36.5	20.63	1	-14.222	2.981	0.067	2	-127.8	1.6	91	O
110	1:34:14.23	30:17:03.3	22.27	1	-14.483	1.196	0.031	2	-125.1	2.4	92	

Table 2—Continued

ID	$\alpha(2000)$	$\delta(2000)$	m_{5007}	$n_p{}^a$	$\log(F_{H\alpha})^b$	$\frac{F([O\ III])}{F(H\alpha)}$	err	$n_s{}^c$	$v_\odot$	σ_v	M01^d	Notes
111	1:34:14.79	30:31:49.6	21.39	2	−14.410	2.285	0.036	2	−159.0	3.0	94	
112	1:34:15.15	30:44:57.4	22.67	2	−14.244	0.480	0.009	3	−211.0	12.1	123	
113	1:34:15.48	30:32:20.3	20.96	2	−14.389	3.221	0.053	1	−153.5	1.1	96	
114	1:34:15.72	31:08:12.5	21.72	1	−14.648	2.903	0.082	1	−276.1	2.9	89	
115	1:34:15.88	30:24:54.5	21.47	2	−14.499	2.597	0.038	2	−160.4	1.0	93	
116	1:34:16.61	30:41:10.4	22.01	2	−14.817	3.272	0.076	2	−225.8	2.1	105	
117	1:34:18.54	30:58:30.5	21.90	1	−14.696	2.752	0.074	2	−287.0	2.6	97	
118	1:34:19.21	30:44:57.0	21.13	2	−14.417	2.940	0.055	2	−257.2	1.9		
119	1:34:20.18	30:51:25.6	23.71	2	−15.070	1.225	0.059	3	−265.6	4.0	98	
120	1:34:20.50	31:10:52.0	22.57	1	−14.370	0.701	0.022	1	$\cdots$			
121	1:34:22.92	31:10:38.6	25.91	1	−16.085	1.686	0.442	1	$\cdots$			
122	1:34:22.96	30:59:32.9	24.07	1	−15.120	0.988	0.067	1	−242.7	12.7	100	
123	1:34:23.01	30:42:06.0	23.84	2	−14.931	0.794	0.040	2	−216.1	6.3	116	
124	1:34:23.26	30:46:27.5	21.45	2	−14.529	2.842	0.049	3	−259.7	1.3	134	
125	1:34:24.26	30:27:54.4	20.98	2	−14.401	3.263	0.041	1	−135.4	1.4	101	O
126	1:34:25.09	30:39:39.7	22.27	3	−14.624	1.652	0.033	1	−240.7	1.5	103	
127	1:34:25.53	30:17:30.0	25.16	1	−15.568	1.017	0.123	3	−145.7	11.6		
128	1:34:25.55	30:40:10.9	21.23	3	−14.429	2.764	0.095	3	−175.3	2.6	104	O
129	1:34:25.83	31:07:44.5	24.28	1	−14.895	0.486	0.032	1	−252.1	9.6	102	
130	1:34:27.71	30:42:32.5	22.25	2	−14.598	1.585	0.044	3	−254.7	2.7	126	
131	1:34:28.00	30:47:45.8	25.00	2	−15.721	1.672	0.255	4	−237.7	9.0		
132	1:34:30.57	30:38:27.3	22.05	3	−14.524	1.607	0.032	2	−154.3	1.3	109	
133	1:34:31.49	31:05:24.0	22.37	1	−14.507	1.158	0.035	1	−252.3	1.7	108	
134	1:34:31.52	31:06:51.3	22.33	1	−14.940	3.242	0.145	2	−262.7	3.2	107	
135	1:34:32.84	30:41:10.6	21.49	2	−14.376	1.916	0.035	2	−188.4	1.0	125	
136	1:34:33.42	30:39:23.7	21.95	2	−14.700	2.657	0.060	2	−208.2	2.2	118	
137	1:34:37.24	30:29:14.3	24.05	1	−15.321	1.605	0.120	1	−145.9	4.7		
138	1:34:37.50	30:40:12.4	24.38	2	−15.255	1.020	0.062	3	−205.8	4.3	129	
139	1:34:37.89	30:27:00.7	21.57	2	−14.432	2.038	0.038	2	−116.8	1.4		
140	1:34:40.70	30:52:08.6	22.84	2	−14.405	0.594	0.015	3	−274.0	5.9	117	
141	1:34:41.96	30:56:49.7	22.41	2	−14.642	1.512	0.029	3	−239.4	1.4	121	
142	1:34:43.57	31:06:10.7	22.51	1	−14.506	1.012	0.033	3	−251.9	4.6	120	
143	1:34:44.72	30:49:36.3	22.11	2	−14.160	0.660	0.012	2	−250.0	8.9	124	
144	1:34:45.50	31:01:11.7	25.81	1	−16.095	1.891	0.363	2	$\cdots$			
145	1:34:46.18	30:44:41.7	22.50	2	−14.960	2.900	0.122	0	−226.8	26.8		O
146	1:34:47.28	30:27:27.5	24.09	1	−14.617	0.307	0.021	2	−160.6	16.9		
147	1:34:58.18	31:06:47.5	22.51	1	−14.634	1.355	0.052	3	−256.1	3.4		
148	1:35:04.92	30:58:42.1	22.54	1	−14.802	1.943	0.068	3	−221.0	1.6		
149	1:35:08.63	30:49:32.8	21.13	2	−14.435	3.062	0.056	1	−213.9	3.7		
150	1:35:09.19	30:51:36.6	21.94	2	−14.752	3.012	0.070	3	−255.0	1.9		
151	1:35:10.50	31:05:14.9	24.41	1	−15.415	1.430	0.128	1	$\cdots$			
152	1:35:13.63	31:00:48.7	21.61	1	−14.467	2.120	0.075	0	$\cdots$			O

^{a}Number of photometric measurements of the PN

^{b}Hα+[N II] flux in units erg cm^{-2} s^{-1}

^{c}Number of HYDRA setups in which PN was targeted (Oct 2002)

^{d}ID number from Magrini et al. (2001)

Note. — O – object also observed in Jan. 2003 observing run; NT – object not targeted spectroscopically; H – possible halo PN

Table 3.   Mean Photometric Errors

[O III] Photometry			Hα Photometry		
m_{5007}	σ(mag)	N_{obj}	log Flux	σ(mag)	N_{obj}
20.75	0.011	9	−14.2	0.012	10
21.25	0.012	21	−14.4	0.018	40
21.75	0.016	16	−14.6	0.022	24
22.25	0.018	24	−14.8	0.026	26
22.75	0.027	24	−15.0	0.035	13
23.25	0.034	14	−15.2	0.051	12
23.75	0.049	19	−15.4	0.072	9
24.25	0.065	14	−15.6	0.100	6
24.75	0.079	3	−15.8	0.133	8

Table 4.   Unconfirmed Magrini et al. (2001) Objects

ID	α (2000)	δ (2000)	Reason
5	1:32:44.04	30:22:04.5	Excess flux in V and B
8	1:32:48.66	30:25:53.2	Excess flux in V and B
10	1:32:54.20	30:37:29.7	Excess flux in V
11	1:33:05.74	30:14:23.3	Non-stellar in [O III]; excess flux in V
20	1:33:09.61	30:29:13.6	Excess flux in V
21	1:33:08.43	30:21:07.2	Nothing at this location; non-stellar object at Magrini et al. (2000) position
23	1:33:13.58	30:22:36.3	Non-stellar in V; excess flux in B
24	1:33:12.25	30:30:49.1	Excess flux in V
34	1:33:24.96	30:38:48.7	Non-stellar in [O III]
44	1:33:33.59	30:39:24.0	Non-stellar in Hα
47	1:34:25.55	30:40:10.7	Coordinates identical to Magrini 104
50	1:33:39.53	30:55:47.1	Excess flux in V
52	1:33:37.37	30:40:54.8	Non-stellar in Hα
53	1:33:41.73	30:37:24.1	Excess flux in V
55	1:33:41.88	30:08:31.3	Excess flux in V
56	1:33:42.80	30:54:04.3	Non-stellar in V; excess flux in Vx
66	1:33:50.88	30:37:12.3	Excess flux in V
70	1:33:54.97	30:37:44.8	Non-stellar in Hα
78	1:34:02.59	30:58:10.2	Non-stellar in [O III]; excess flux in V
87	1:34:12.05	30:39:10.1	Excess flux in V
90	1:34:12.82	30:47:18.1	Non-stellar in Hα
99	1:34:20.61	30:16:47.5	Non-stellar in Hα
114	1:34:16.39	30:43:26.5	Non-stellar in Hα; excess flux in V
115	1:34:09.90	30:45:07.8	Non-stellar in [O III]
122	1:33:37.89	30:39:34.8	Non-stellar in [O III] and V; excess flux in V
127	1:34:47.13	30:59:36.9	Non-stellar in Hα; excess flux in V
128	1:34:48.86	31:05:14.8	Non-stellar in Hα; excess flux in V
131	1:34:51.19	30:59:34.8	Non-stellar in Hα; excess flux in V
132	1:34:49.20	30:37:27.7	Excess flux in V and B
133	1:34:35.30	30:43:56.5	Excess flux in V

Table 5.   Setup Velocity Differences

Setups	$\overline{\Delta v}$	σ_{pair}	N
$1-2$	-0.9	1.0	5
$1-3$	-1.5	2.7	8
$1-4$	-3.7	4.9	22
$1-5$	$+0.7$	3.3	22
$1-6$	-0.3	7.2	17
$2-3$	$+0.8$	8.6	18
$2-4$	-7.9	6.4	6
$2-5$	-3.2	6.4	19
$2-6$	-0.4	5.3	12
$3-4$	-6.0	4.9	13
$3-5$	-5.6	5.8	9
$3-6$	-2.6	4.8	16
$4-5$	$+2.6$	3.3	10
$4-6$	$+1.0$	6.3	21
$5-6$	$+1.6$	7.7	11

Table 6.   M33 Disk Mass and Mass-to-Light Ratios

Radius (kpc)	Surface Mass ($M_\odot$ pc^{-2})	M/L_K	M/L_V	(Stellar) M/L_V
1.2	$79.2^{+49.3}_{-39.4}$	$0.22^{+0.14}_{-0.11}$	$0.52^{+0.33}_{-0.26}$	$0.25^{+0.19}_{-0.15}$
2.1	$54.1^{+31.4}_{-24.5}$	$0.25^{+0.15}_{-0.11}$	$0.50^{+0.29}_{-0.22}$	$0.26^{+0.19}_{-0.15}$
2.7	$82.3^{+33.3}_{-28.5}$	$0.59^{+0.24}_{-0.21}$	$1.00^{+0.41}_{-0.35}$	$0.63^{+0.29}_{-0.25}$
3.4	$51.8^{+21.3}_{-18.1}$	$0.60^{+0.25}_{-0.21}$	$0.85^{+0.35}_{-0.30}$	$0.55^{+0.27}_{-0.23}$
4.5	$31.6^{+13.3}_{-11.2}$	$0.74^{+0.31}_{-0.26}$	$0.82^{+0.34}_{-0.29}$	$0.50^{+0.29}_{-0.25}$
6.0	$31.0^{+9.3}_{-8.3}$	$1.79^{+0.54}_{-0.48}$	$1.42^{+0.43}_{-0.38}$	$0.99^{+0.39}_{-0.34}$
7.1	$19.2^{+6.1}_{-5.4}$	$2.34^{+0.74}_{-0.66}$	$1.42^{+0.45}_{-0.40}$	$0.98^{+0.42}_{-0.37}$
8.5	$16.3^{+5.0}_{-4.5}$	$4.68^{+1.44}_{-1.29}$	$2.07^{+0.64}_{-0.57}$	$1.52^{+0.61}_{-0.55}$
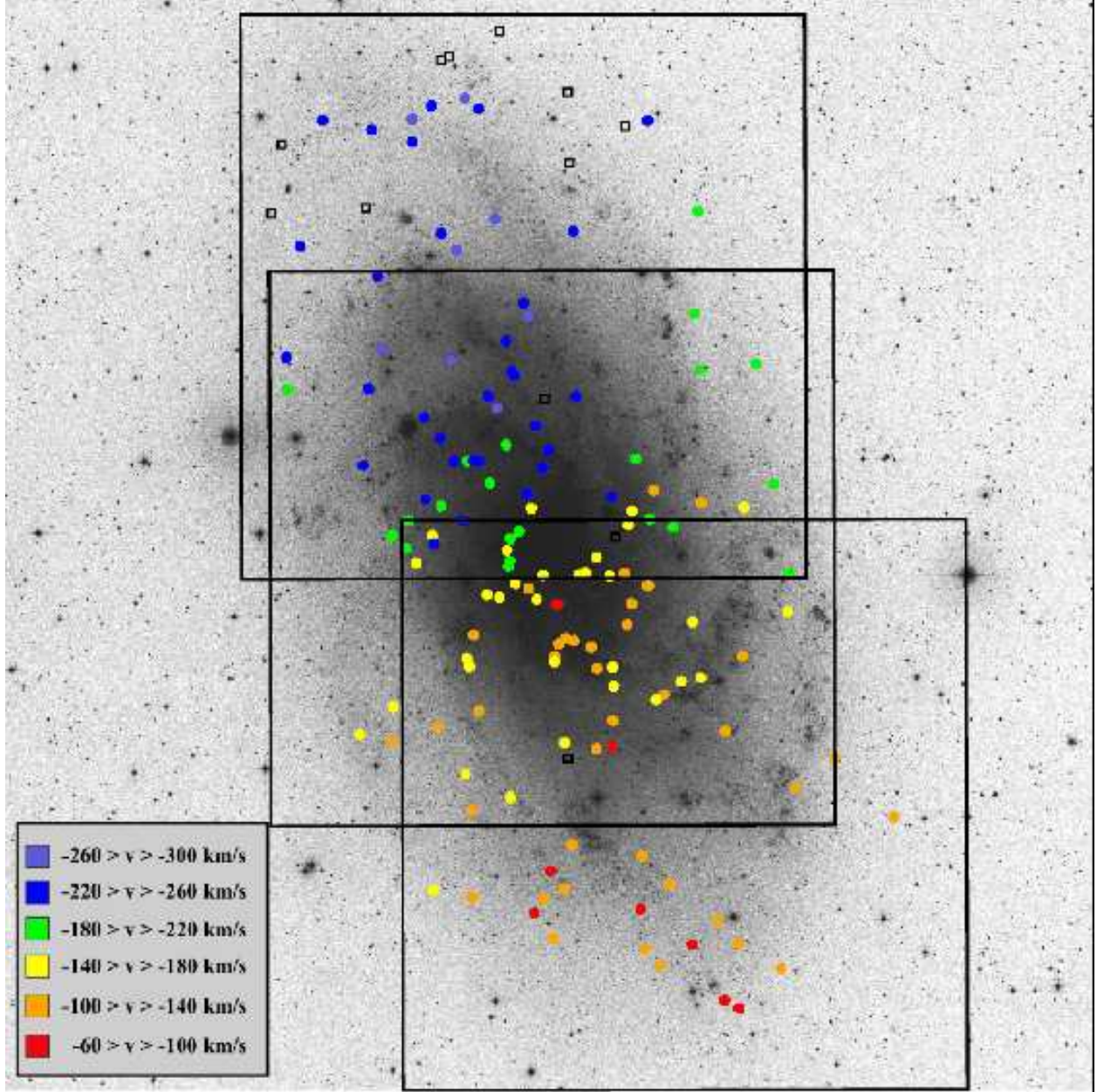
Fig. 1.— A Digital Sky Survey image of M33. North is up and east is to the left; the image is 1°1 (18 kpc) on a side. The positions of our 152 PN candidates are marked with boxes. PNe measured spectroscopically with WIYN are color-coded to show their heliocentric radial velocity.
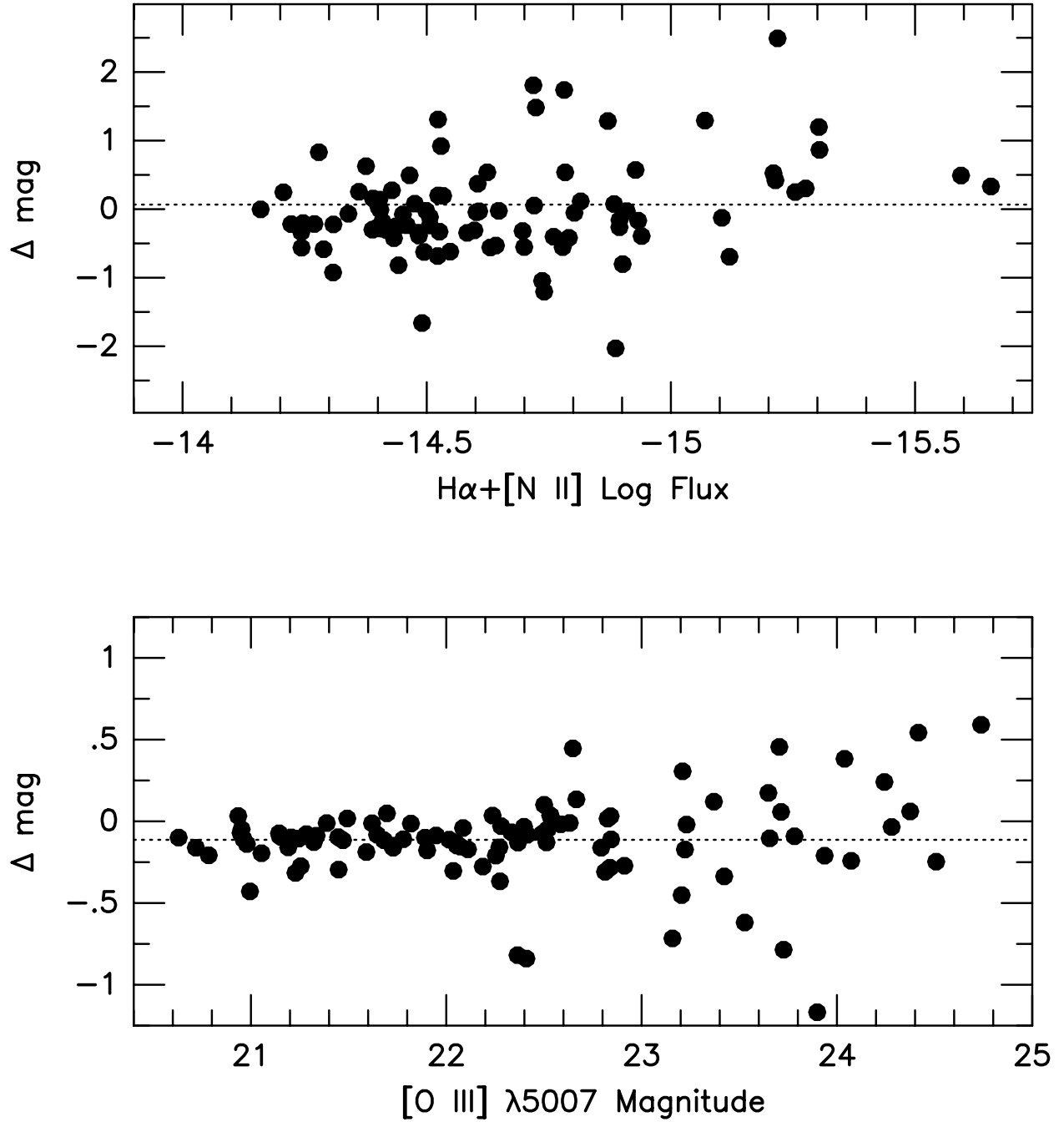
Fig. 2.— A comparison of our [O III] $\lambda5007$ and Hα+[N II] photometric measurements against those of Magrini et al. (2001) for the 101 planetary nebulae common to both surveys. For the brighter objects ($m_{5007} \lesssim 23$), the relative [O III] magnitudes are in good agreement, though our measurements are systematically brighter by 0.12 mag. The agreement for Hα is somewhat poorer: although our magnitudes are systematically fainter by only 0.06 ± 0.05 mag, the scatter for individual measurements is ~ 0.25 mag.
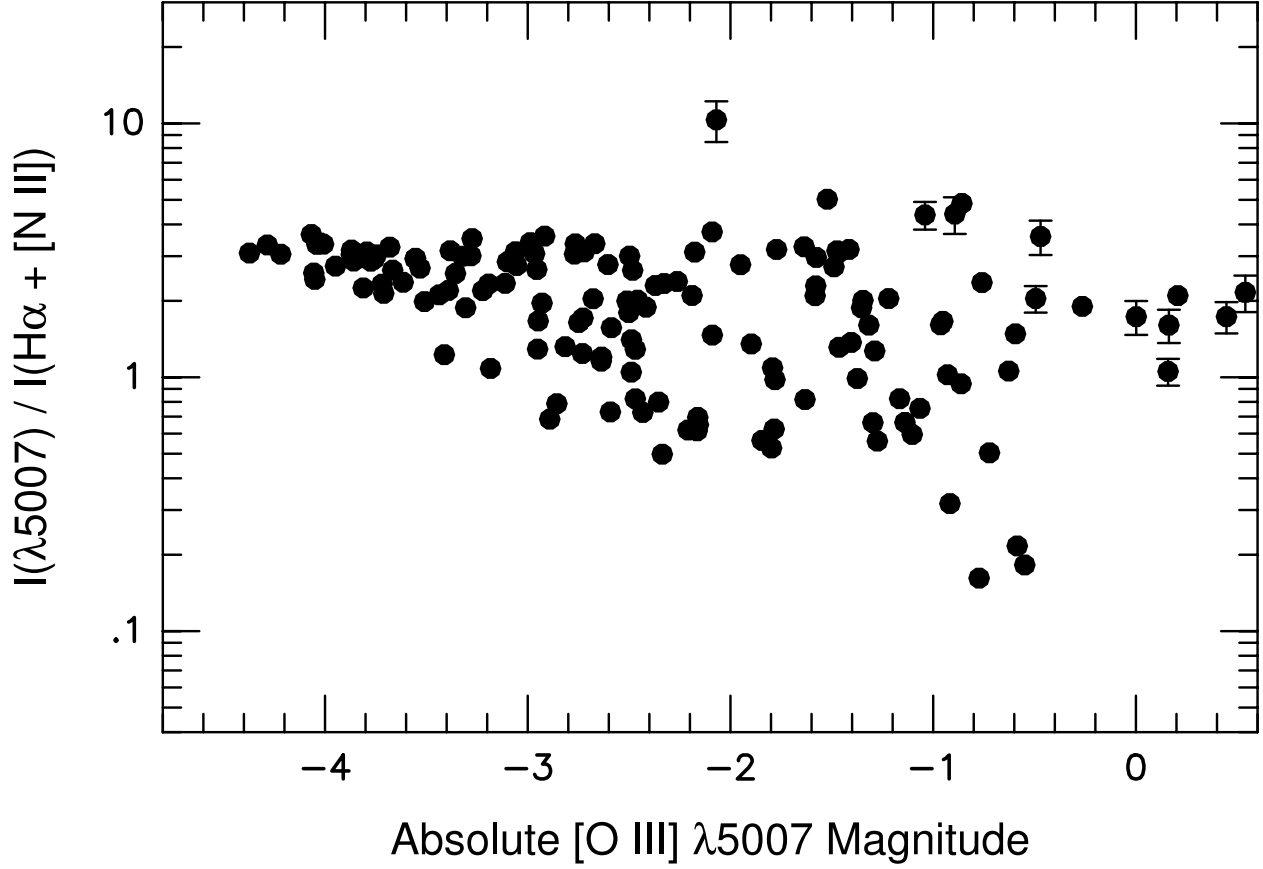
Fig. 3.— The [O III] λ5007 to Hα+[N II] line ratios for PNe in M33. The measurements have been corrected for the effects of foreground Galactic extinction, but not circumstellar extinction or extinction internal to M33. For most PNe, the photometric uncertainties are smaller than the size of the plotted points and have not been displayed. The region of emission-line space occupied by planetary nebulae has a distinctive shape that is the same for all stellar populations.
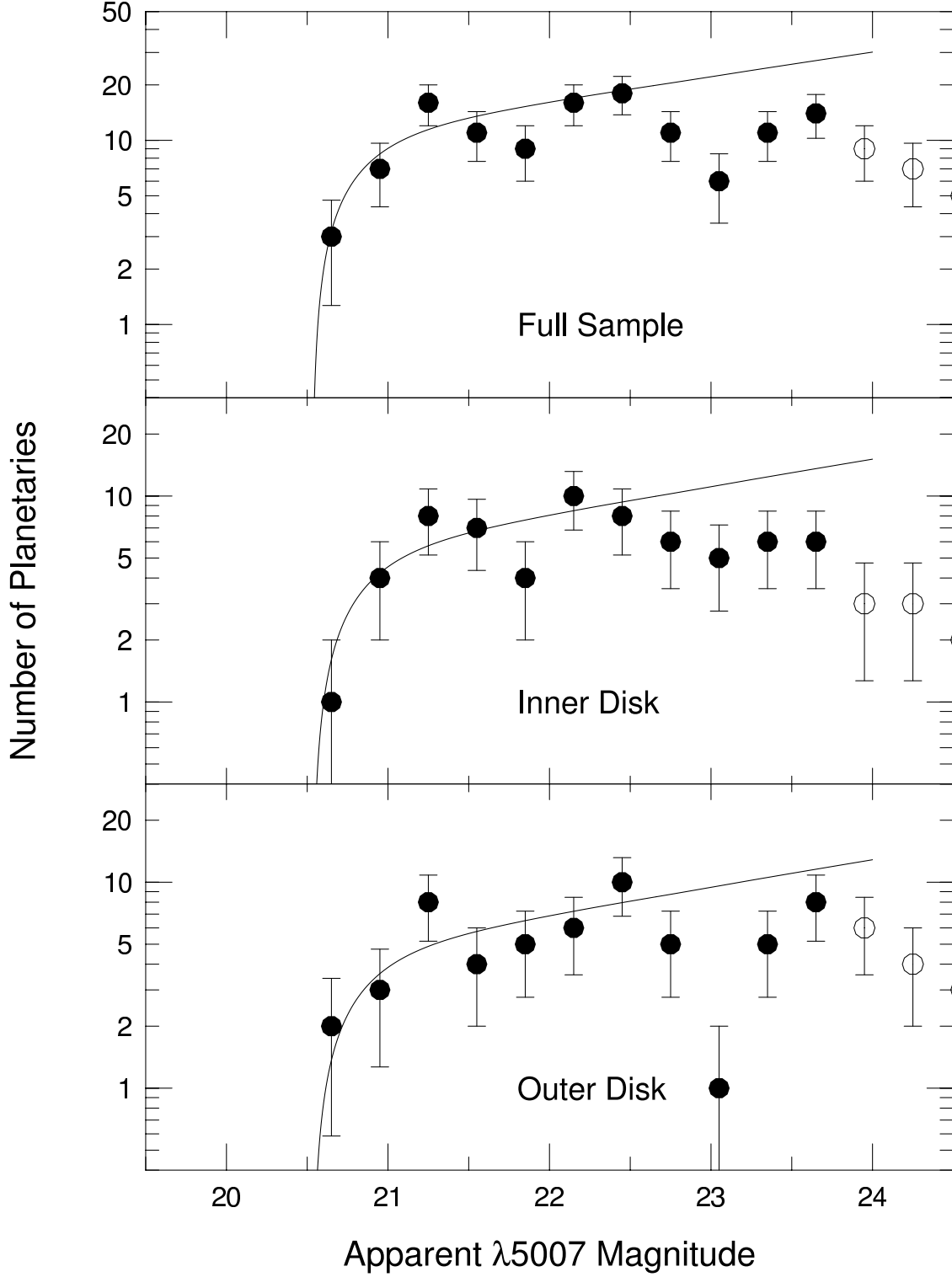
Fig. 4.— The [O III] $\lambda5007$ planetary nebula luminosity function of M33. The top panel displays the entire PN sample, the middle panel shows only those PNe within $15'$ of M33's nucleus, and the lower panel includes only the PNe outside this isophotal radius. The curve shows the analytic PNLF convolved with the photometric error function and shifted to the most-likely distance of the galaxy. The open circles represent points past the completeness limit. Note that the luminosity functions of M33's inner and outer disk are statistically indistinguishable, and that the PNLF turns over well before the completeness limit is reached.
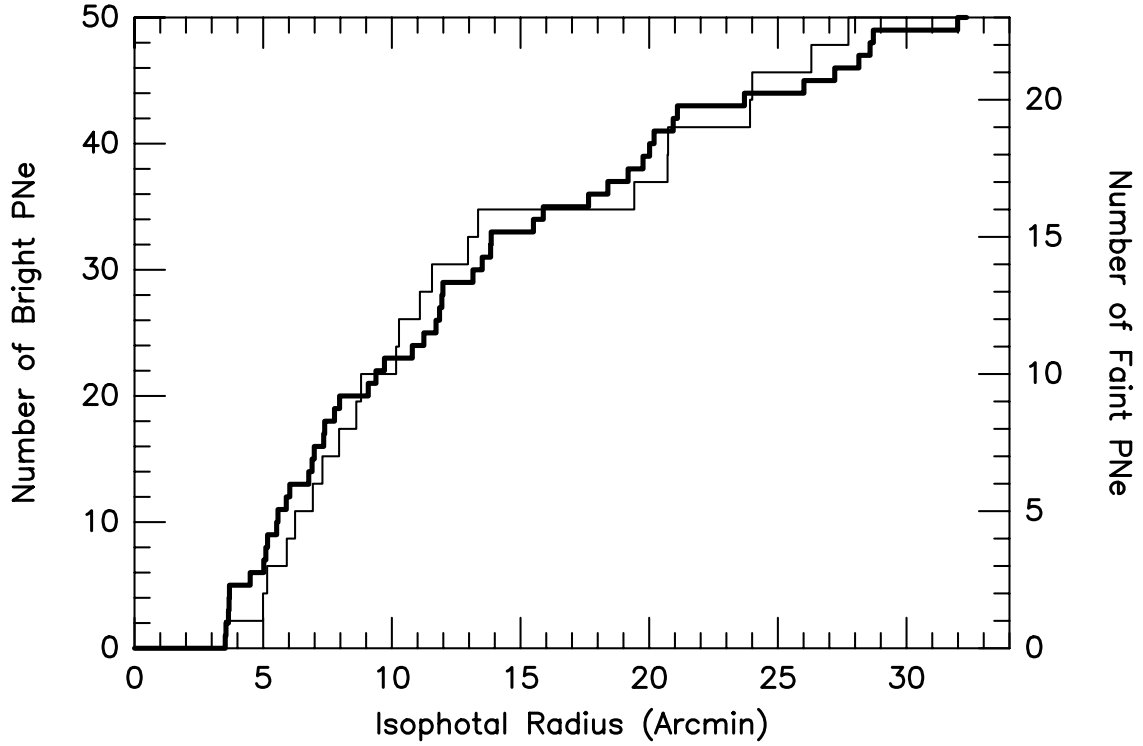
Fig. 5.— The solid dark line is the cumulative distribution of isophotal radii for a sample of "bright PNe" with $m_{5007} < 22.5$. The lighter line is a similar distribution for PNe well past the luminosity function turnover, i.e., with $23.0 \leq m_{5007} \leq 23.75$. The two distributions are statistically identical. The agreement confirms that our PN sample is complete to $m = 23.75$ to within $3\overset{\prime}{.}5$ of the nucleus.
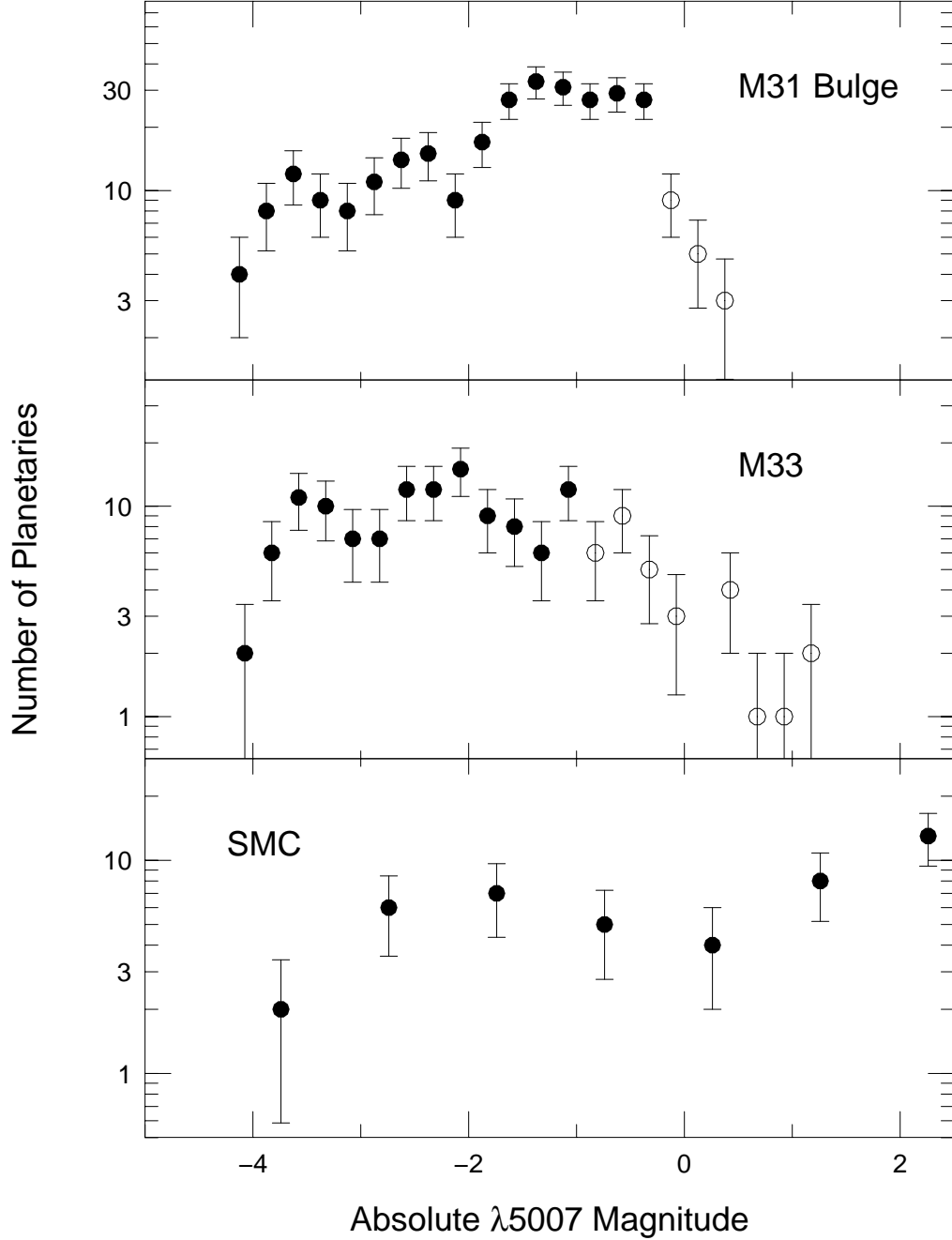
Fig. 6.— The [O III] λ5007 planetary nebula luminosity functions of three Local Group stellar populations. The data for M31's bulge are taken from Ciardullo et al. (2002); the SMC luminosity function comes from Jacoby & De Marco (2002). The absolute magnitudes are derived using the Cepheid distances to the galaxies (Freedman et al. 2001; Udalski et al. 1999) and the Galactic extinctions given by Schlegel, Finkbeiner, & Davis (1998). While the PNLF of M31's bulge is a monotonically increasing function, the luminosity functions of the two star forming systems decline at fainter magnitudes.
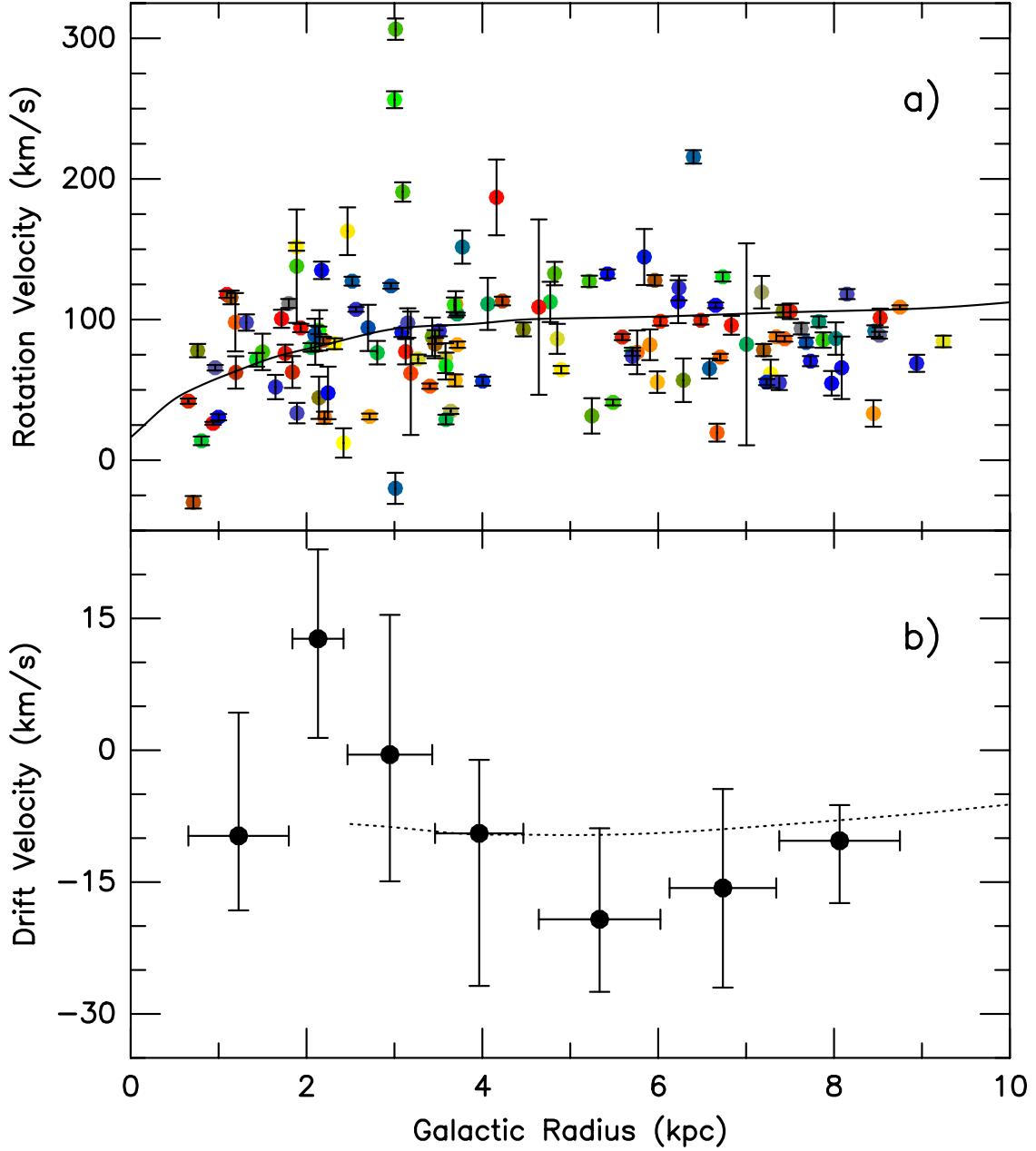
Fig. 7.— The upper panel compares the inferred rotation speeds of M31's planetaries with the rotation of the galaxy's H I and CO gas. The colors denote the azimuthal position of the PNe: the color sequence blue through green through red through yellow through blue represents angles of 0° through 90° through 180° through 270° through 360° from the approaching major axis. Fourteen PNe projected within 10° of the system's minor axis have not been plotted. Note that the scatter in the diagram is significantly larger than the measurement errors for individual objects. Note also that, in the mean, the PNe rotate slightly slower than the gas; this is due to asymmetric drift. The lower panel bins the data (with 18 PNe per bin) to show the variation of the drift velocity with galactocentric radius. Here, the error-bars in y represent the $1\,\sigma$ uncertainty, as determined via a bootstrap analysis, while the error bars in x illustrate the size of the bin. The dotted line is our best-fit model for regions outside 2.5 kpc (see Section 7).
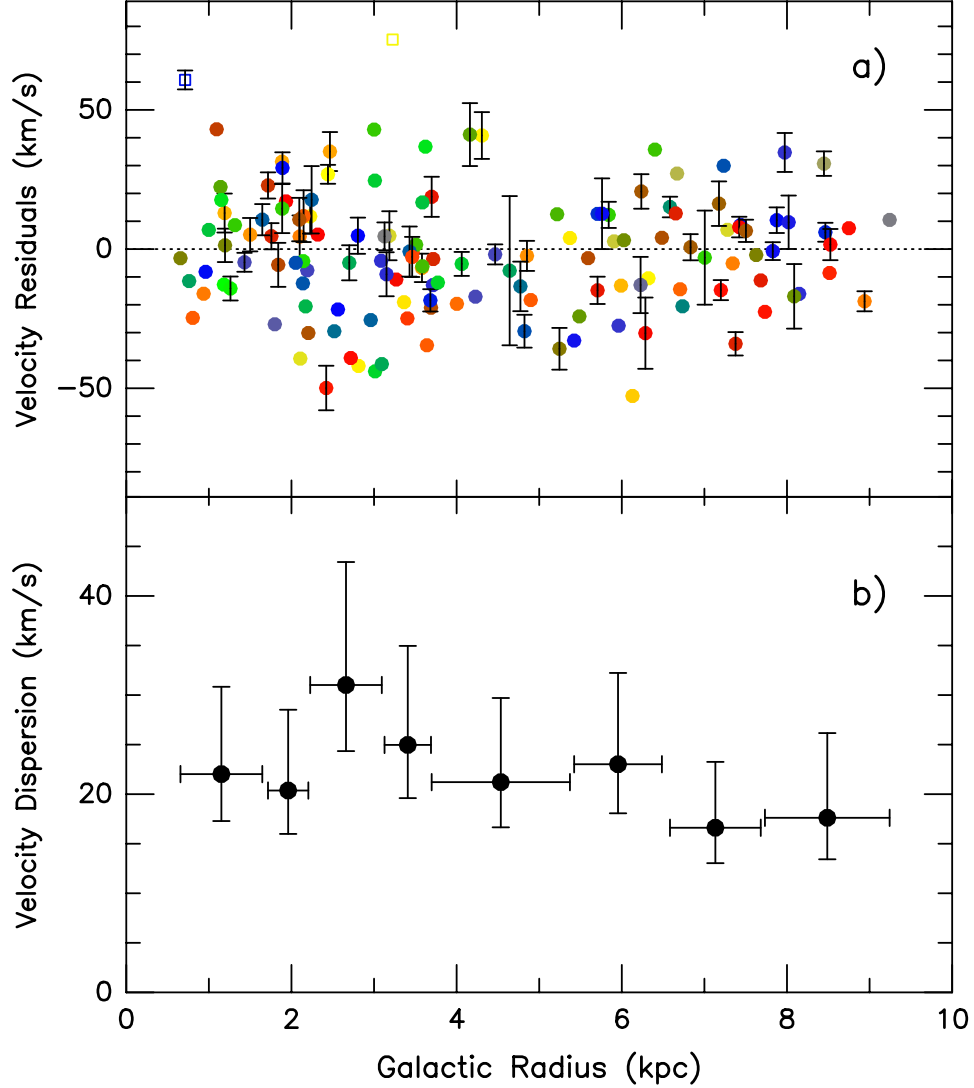
Fig. 8.— The upper panel plots the PN radial velocities with the galaxy's systemic velocity and disk rotation (defined as the H I rotation speed minus asymmetric drift) removed. Error bars have only been plotted for objects with random velocity uncertainties greater than 3 km s^{-1}; the two possible halo planetaries are shown as open squares. As in Figure 7, the colors represent the azimuthal position of each planetary, with the color sequence blue through green through red through yellow through blue denoting angles of 0° through 360° (referenced from the approaching major axis). The lower panel bins the data (with 18 PNe per bin) to show how the line-of-sight velocity dispersion varies with galactocentric radius. The errors in y represent 90% confidence intervals, while the error bars in x illustrate the size of each bin.
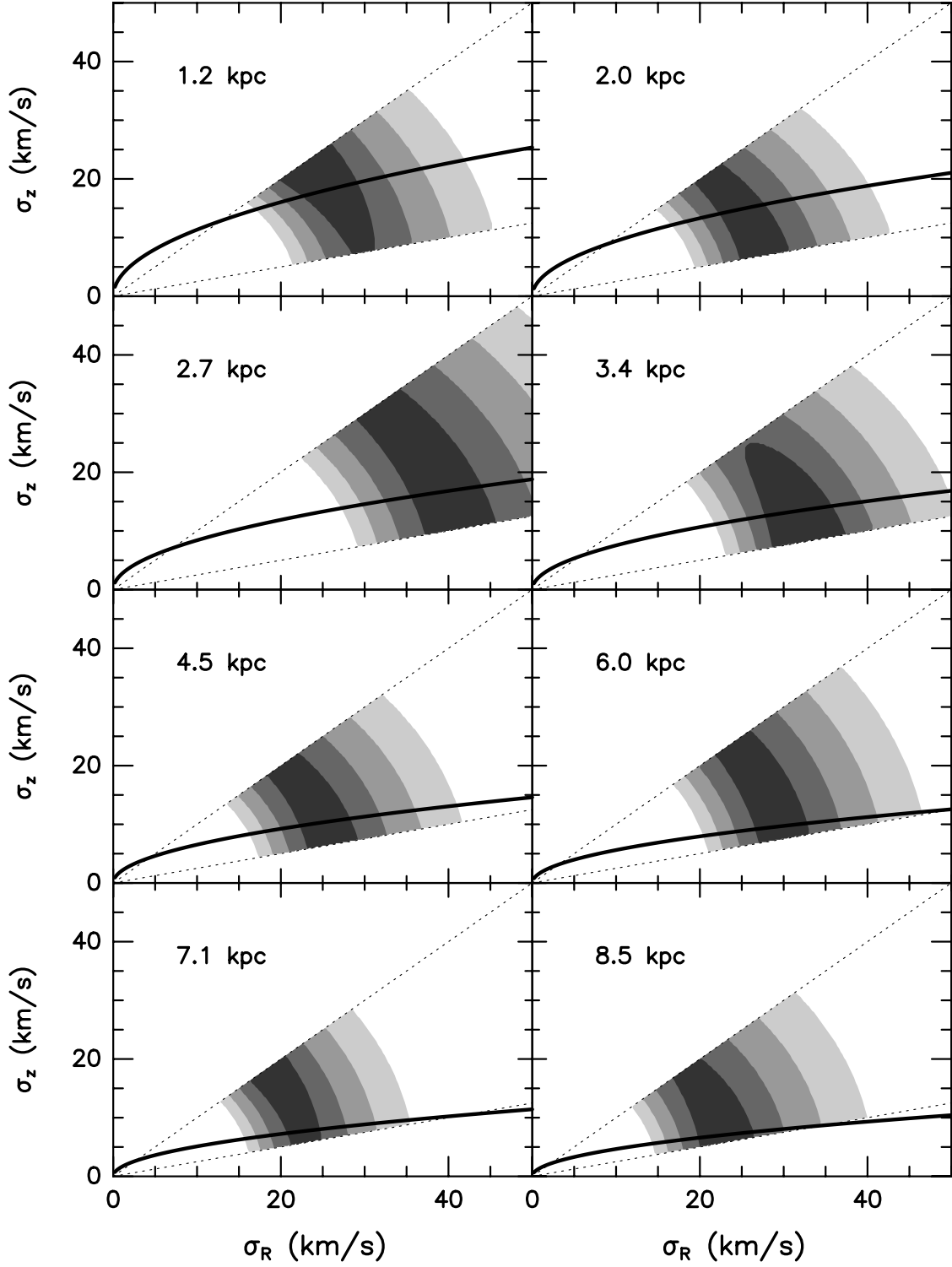
Fig. 9.— Maximum likelihood solutions for the light-of-sight radial velocity dispersions in the 8 radial bins displayed in Figure 8. From dark to light, the shaded regions enclose 38% (0.5σ), 68% (1σ), 86% (1.5σ), and 95% (2σ) of the probability. The solid line displays the limits placed on the solutions by the requirement that the disk be stable against axisymmetric and non-axisymmetric perturbations; the dotted lines show the limits of our analysis. Note that at large radii, the stability criterion strongly constrains the shape of the velocity ellipsoid and σ_z.
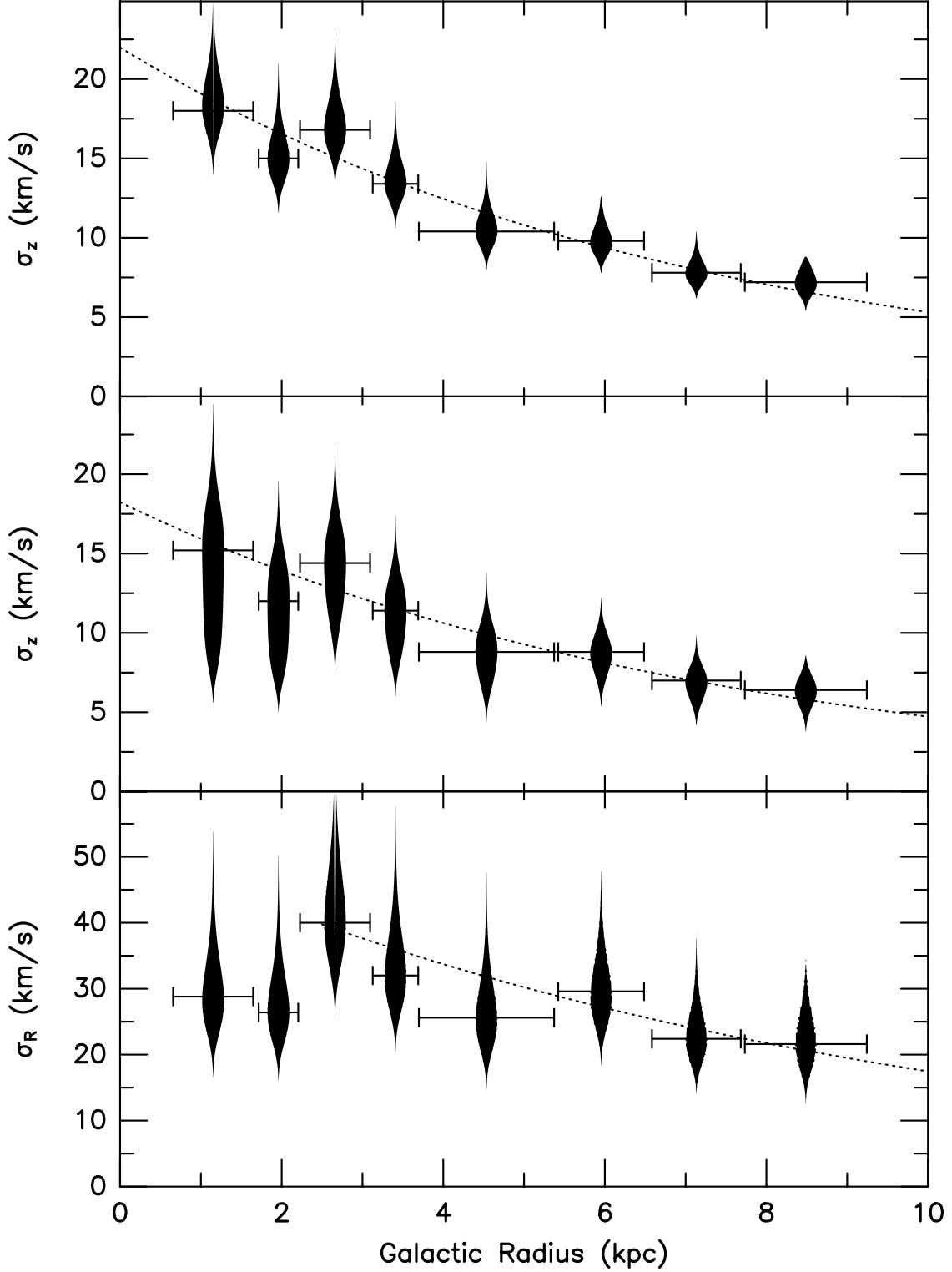
Fig. 10.— The likelihoods of Figure 9, constrained by the requirement of stability, and marginalized into one-dimensional plots in σ_z and σ_R. The non-Gaussian uncertainties are illustrated by the width of the lines. The dotted lines show the best-fit exponentials, when the additional constraints provided by our asymmetric drift measurements are imposed (see text). The middle and lower panels show total likelihoods; the upper panel illustrates the solution for a marginally stable (maximum mass) disk. The implied scale length of σ_z^2 is more than twice as large as that of the K-band light.
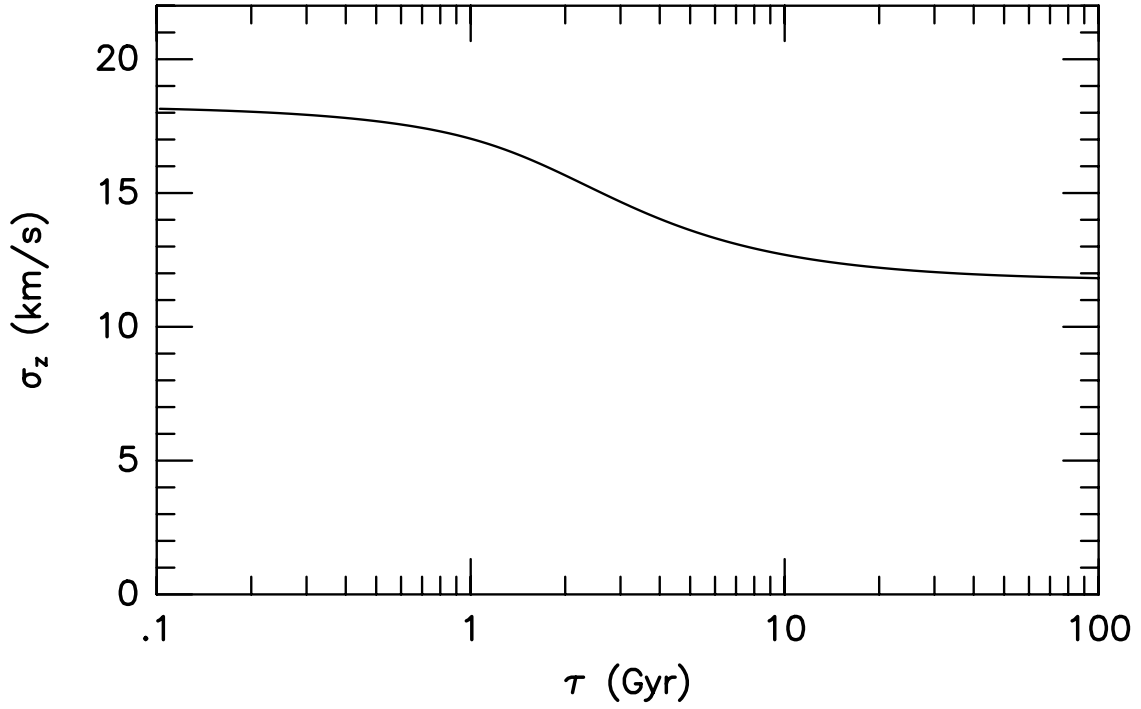
Fig. 11.— The vertical velocity dispersion of disk planetary nebulae as a function of the exponential decay time of star formation. The plot assumes a Scalo (1986) initial mass function that is constant with time, the Iben & Laughlin (1989) initial mass-stellar lifetime relation, and that $\sigma_z \propto t^{1/2}$. The y-axis has been arbitrarily normalized to 20 km s^{-1} at 10^{10} yr. Note that disks with a constant star formation rate ($\tau \gg 1$) have velocity dispersions that are a third smaller than disks whose star formation has long ago decayed away.
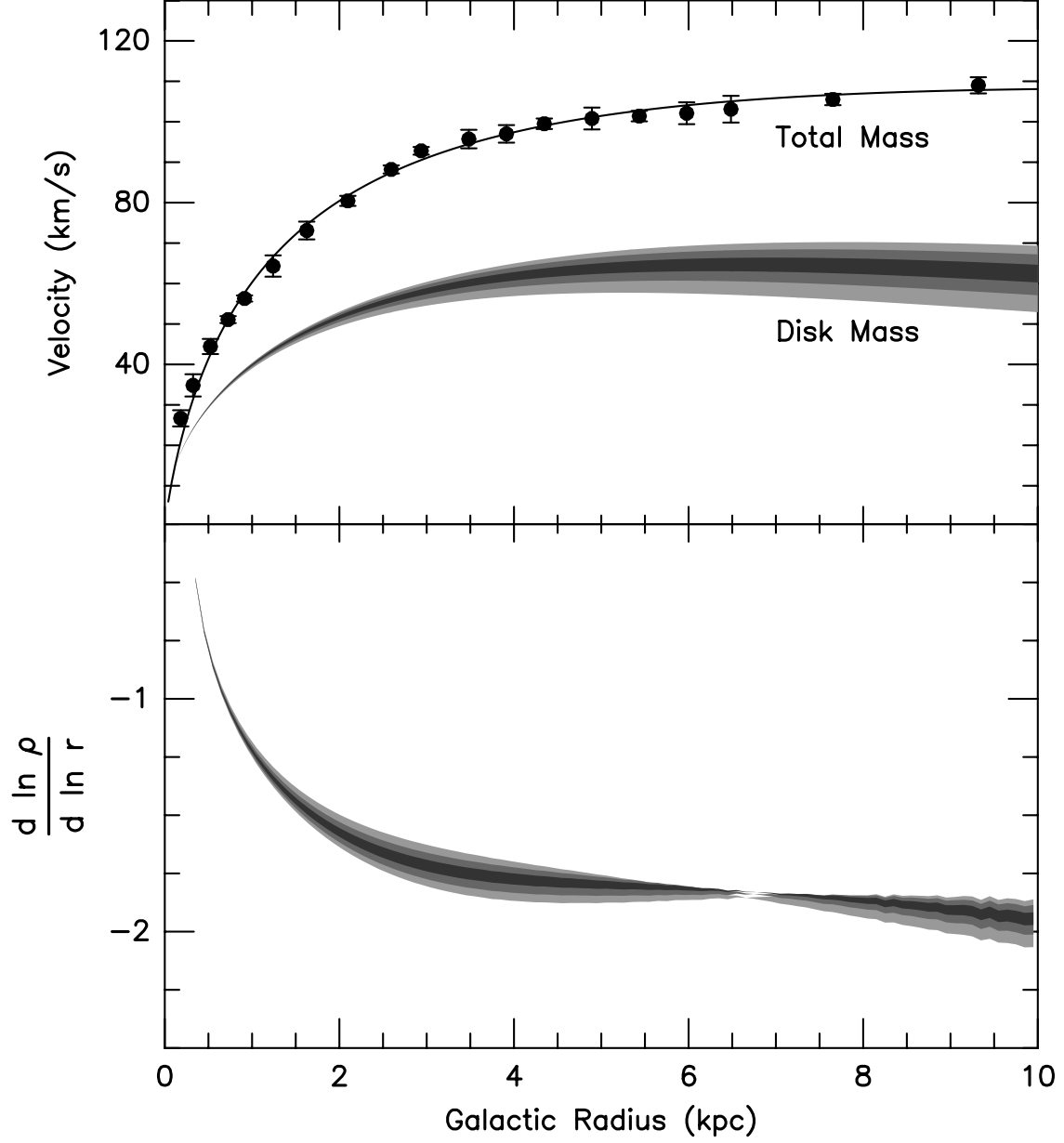
Fig. 12.— The upper panel compares M33's H I and CO rotation curve to the rotation curve which would be produced from the disk alone. The solid line is a Brandt (1960) law fit to the H I and CO velocity measurements; the shaded regions indicated the 1, 2, and 3σ uncertainties about our best-fit mass model (as determined from a jackknife analysis). The lower panel shows the density law inferred for the galaxy's dark halo (under the assumption of spherical symmetry), again with 1, 2, and 3σ uncertainties.